The Role of the Overriding Plate and Mantle Viscosity Structure on Deep Slab Morphology

Antoniette Greta Grima [1], Carolina Lithgow-Bertelloni[2]and Fabio Crameri[3]

[1]School of Geographical & Earth Sciences, University of Glasgow, Molema Building, Lilybank Gardens, Glasgow, G12800, United Kingdom
[2]Department of Earth, Planetary, & Space Sciences, University of California, 595 Charles Young Drive East, Los Angeles, CA 90095, California, USA
[3]Undertone Design, Bern, Switzerland

Key Points:

- Deep slab morphologies and dynamics are an expression of overriding plate type and lower mantle viscosity structure.
- A continental upper plate and a lower mantle viscosity increase at 1000 km encourage renewed deep slab steepening and lower mantle penetration.
- Slab behaviour can be described by the ratio of deep slab tip angle and the subduction angle at the trench.

Corresponding author: Antoniette Greta Grima, antoniettegreta.grima@glasgow.ac.uk

Abstract

Using 2D numerical subduction models, we compare deep slab behaviour with oceanic and continental overriding plates and a mantle viscosity structure where the lower mantle viscosity jump occurs either at 660 km or at 1000 km depth as suggested by the latest geoid inversions. We demonstrate that a strong, thick, and buoyant continental plate, combined with a 1000 km depth viscosity increase, promotes slab penetration into the lower mantle. Conversely, the same slab will deflect at 660 km depth if this subducts under an oceanic plate into a mantle where the viscosity increases at the canonical 660 km depth. To quantify these dynamics, we introduce a slab bending ratio, by dividing the deep slab tip angle by the shallow slab angle, reflecting the steepness, and sinking history of the slab. Ocean-ocean convergence models with a viscosity increase coincident with the phase transition at 660 km depth have low ratios and flattened slabs comparable to ocean-ocean cases in nature (e.g., Izu-Bonin). Coupling a continental overriding plate with a 1000 km depth viscosity increase separate from the endothermic phase change results in slabs with high ratio values, and stepped morphologies similar to that observed for the Nazca plate beneath the Southern Peruvian arc. Our results highlight that slab morphologies ultimately express the interaction between the type of overriding plate, slab-induced flow, and phase transitions, modulated by the viscosity structure of the top of the lower mantle and transition zone.

Plain Language Summary

Ocean floors that sink as slabs into the mantle exhibit varied shapes. Some flatten at the top of the lower mantle while others sink deeper, taking on a "stepped" form. Slab dynamics at these depths regulate the amount of mass transferred across the mantle and can be described by the ratio of the slab tip's angle and the angle of the shallow slab closer to the surface. We find that the type of overriding plate and the depth at which the viscosity in the lower mantle increases, influences the slab angle ratio to determine the slab's shape and its depth. When the overriding plate is continental and the mantle viscosity jump occurs at greater depths, the angle ratio values are large and the slab sinks steeply into the lower mantle. We show that the slab shape is determined by a combination of surface plate interactions, the mineral physics within and around the slab, and the mantle structure at depth. Our findings can be applied to slabs at different subduction zones and explain why some slabs flatten and while others penetrate in to the lower mantle. This valuable insight explains how the interior of the Earth dynamically links with its surface.

1 Introduction

Subduction is the sinking of oceanic lithosphere underneath an overriding plate into the mantle beneath it. This occurs for both thin, neutrally buoyant, and thick, positively buoyant overriding plates. Recent work by (e.g., Butterworth et al., 2012; Sharples et al., 2014; Holt, Becker, & Buffett, 2015) shows that the inclusion of an overriding plate in numerical models produces a better fit to observations, with overriding plate models exhibiting slab and trench rollback velocities comparable to those observed in nature. This highlights the important role of the overriding plate in modulating subduction dynamics at shallow depths.

Work by Conrad & Lithgow-Bertelloni (2006); Naliboff et al. (2009); Willingshofer et al. (2013); Sharples et al. (2014); Holt, Buffett, & Becker (2015) and Holt, Becker, & Buffett (2015) shows that beyond its presence, the nature of the overriding plate is also important; where buoyant and strong continental lithosphere enhances global plate driving forces by strengthening basal mantle tractions beneath the lithospheric plates, encourages increased surface deformation through more pronounced uplift and subsidence,

and produces steeper slab angles at the trench (Zhong & Gurnis, 1995; Zhong, 2001; Heuret & Lallemand, 2005; Conrad & Lithgow-Bertelloni, 2006; Summeren et al., 2012; Zahirovic et al., 2015).

The overriding plate thickness may also influence the subducting plate dynamics and deep slab morphology, with thick overriding plates encouraging overall steeper slabs, decreased trench mobility and increased slab penetration into the lower mantle (Garel et al., 2014; Sharples et al., 2014; Holt, Becker, & Buffett, 2015; Crameri & Lithgow-Bertelloni, 2018). However, in most of these studies except for (e.g., Crameri & Lithgow-Bertelloni, 2018), overriding plate variations are limited to differences caused by age variations and exclude the differences in strength, density, and buoyancy expected with continental overriding plates. As far as we are aware, no studies have explored the role of continental density and strength variations on deep slab dynamics. Similarly, depth variations in background mantle viscosity are limited to a viscosity jump at 660 km depth. This approach commonly adopted by previous work, is based on inversions of post-glacial rebound and the gravity field with a prescribed viscosity jump (e.g,. Hager, 1984; Billen & Hirth, 2007; Garel et al., 2014). However, beyond the general increase in lower mantle viscosity, published viscosity profiles of the mantle are non-unique. Previous work finds that when the viscosity jump is not prescribed to occur at 660 km depth, the increase in viscosity occurs much closer to $\sim$ 900–1,200 km depth (King & Masters, 1992; Mitrovica & Forte, 2001, 2004; Rudolph et al., 2015, 2020). In this work we therefore explore the effects of both a viscosity jump at 660 km depth as well as a deeper increase in viscosity at 1000 km depth. We combine these two viscosity profiles with different overriding plate types and expand on previous efforts to better constrain the behaviour of slabs at the top the lower mantle.

2 Methods

2.1 Modelling approach

We use generic numerical forward models (Van Zelst et al., 2022) to model ocean-ocean and ocean-continent subduction within a standard mantle viscosity structure, where the viscosity increases at 660 km depth (reference model V1) and compare this against subduction models where the mantle viscosity increase occurs at 1000 km depth (model V2) for both oceanic and continental overriding plate setups.

2.2 Physical Model and Rheology

Our methodology, set-up and implementation follows that of Crameri & Lithgow-Bertelloni (2018) andGrima et al. (2020). We use the multigrid finite difference/volume code StagYY (Tackley, 2008) to solve the non-dimensional equations for the conservation of mass (eq. 1), momentum (eq. 2), and energy (eq. 3), to model flow in an incompressible viscous fluid under the Boussinesq approximation, with negligible inertia.

$$\nabla \cdot v = 0 \tag{1}$$

$$\nabla \cdot \sigma_{ij} - \nabla P = Ra(1 + P_B \cdot \frac{\delta\Gamma}{\delta\phi}) \cdot T\hat{e}_z \tag{2}$$

$$\frac{\delta T}{\delta t} = \nabla^2 T - v \cdot \nabla T + H \tag{3}$$

where v is the velocity, σ_{ij} is the deviatoric stress tensor, P the pressure, T is the temperature, $\hat{e}_z$ the vertical unit vector, t the time and H the non-dimensional inter-

nal heating rate and P_B the phase buoyancy parameter (Christensen & Yuen, 1985) defined as:

$$P_B = \frac{\gamma \delta \rho}{g \alpha \rho^2 D} \tag{4}$$

γ is the Clapeyron slope, Γ is the phase function ($0 \leq \Gamma \leq 1$) indicating the relative portion of the dense phase, ϕ the excess pressure (*c.f.,* Christensen & Yuen, 1985) given by:

$$\phi = P - (P_0 + \gamma T) \tag{5}$$

P is the hydrostatic pressure, and P_0 is the transition pressure at 0 K. For an in-depth description of the buoyancy parameter and the phase function implementation used in this study please refer to Grima et al. (2020) and see Table 1 for the values used in this work.

The Rayleigh number Ra is expressed as:

$$Ra = \frac{\rho g \alpha \Delta T D^3}{\eta_0 \kappa} \tag{6}$$

where ρ is the density, g is the gravitational acceleration, α is the thermal expansivity, $\Delta\ T$ the temperature scale, D is the depth of the mantle, κ the thermal diffusivity and η_0 is the reference viscosity. Following from eq. 6 and the values in Table 1, the Ra in our models has a value of 10^7. We apply an internal heating rate of $4.92{\cdot}10^{-12}$ Wkg^{-1}, which is equivalent to a non-dimensional value of 18.08 and results in an internal heating-based Rayleigh number of $1.8\ \cdot\ 10^8$ (e.g., Turcotte & Schubert, 2014).

The composite viscosity of our models includes diffusion and dislocation creep and plastic yielding:

$$\eta_i(P,T) = \eta_0 \cdot \eta_b(P)\left(\frac{\sigma^{1-n_i}}{\sigma_{TS}} exp\left[\frac{E_i^* + PV_i^*}{RT}\right]\right) \tag{7}$$

where $\eta_b(P)$ contains the viscosity jumps either at 660 km depth or at 1,000 km depending on the model set-up. $E*$ and $V*$ are the activation energy and volume, respectively, R is the gas constant, and n is the stress/power law exponent (Table 1). Subscripts i refer to the two creep mechanisms; diffusion or dislocation creep. σ_{TS} is the activation stress value for dislocation creep (Table 1). For diffusion creep, the power-law exponent n is equal to 1.

The effective viscosity is therefore:

$$\eta_{eff} = min\left[\left(\frac{1}{\eta_{diffusion}} + \frac{1}{\eta_{dislocation}}\right)^{-1}, \eta_y\right] \tag{8}$$

where the limiting plastic viscosity η_y combines a Drucker-Prager yield criterion for brittle failure and a homogeneous ductile yield stress limit S which is applied everywhere throughout our model except for the sticky-air layer and is described by:

$$\eta_y = \left(\frac{1}{2\epsilon}\right) min[C + P\mu, S] \tag{9}$$

where C is the cohesion, ϵ is the strain rate and the friction coefficient is μ (Table 1). For numerical stability the viscosity is bound by an upper and a lower limit of $10^{-4} \leq \eta_{eff} \leq 10^{5}\ \eta_0$.

In agreement with previous work (Hager, 1984; Hager & Richards, 1989), we increase the viscosity of the lower mantle in our models by implementing a viscosity jump of an order of magnitude at 660 km depth for our reference model and compare this with a case where the viscosity increase (of the same magnitude) occurs at 1000 km depth (Fig. 1) as suggested by the recent geoid inversions of Rudolph et al. (2015, 2020).

Similar to Grima et al. (2020) and Crameri & Lithgow-Bertelloni (2018), our models include a weak hydrated crustal layer on top of subducting lithosphere which is $\approx$ 10 Myr old and forms a freely evolving weak subduction channel once the plate subducts (Crameri & Tackley, 2015). This weak crustal layer is 15 km thick and has a lower yield stress compared to mantle material. Once the weak crustal layer reaches a depth of 400 km, it is converted to regular mantle material. We also include a melting viscosity reduction (MVR) to simulate a low-viscosity asthenosphere underneath the subducting and overriding plates. The MVR describes a factor 10 decrease in viscosity in regions where the temperature exceeds a simple linear, depth-dependent solidus (Tackley, 2000).

We also include a continental overriding plate that is 200 km deep and 2000 km wide. The continental roots extend to the bottom of the asthenosphere and the continental geometry is rectangular with an angled edge at the trench following the implementation of Crameri & Lithgow-Bertelloni (2018). The continental material is chemically and compositionally identical to the mantle material underneath but is distinguishable by its lower density, determined by its buoyancy ratio B_c. B_c describes the density contrast of the continent $\Delta\ \rho_c$ with respect to the ambient mantle $\Delta\rho_m$, divided by the thermal density variation $\rho\alpha\Delta T$ such that $B_c = \frac{\Delta\rho_c - \Delta\rho_m}{\rho\alpha\Delta T}$. We assume a continental density of 3250 kgm^{-3} and take an average mantle density of 3300 kgm^{-3}, which produces a continental density contrast $\Delta\ \rho_c$ of -25 kgm^{-3} and a buoyancy ratio B_c of -0.10. Negative B_c values imply a light and more buoyant continent. We also increase the viscosity to 10^{24} and the friction coefficient of the continental lithosphere to 0.5, which translate to a higher ductile strength and implies that within the continental lithosphere yielding occurs for much higher stresses than the rest of the model. This makes the continent both lighter and stronger compared to the underlying mantle and the oceanic lithosphere.

2.3 Numerical Model Set-up

Our set-up (Fig. 1) follows from Grima et al. (2020) and our models evolve dynamically and self-consistently without any external forces or velocities applied to the system. Our models have a 2D geometry with an aspect ratio of 2:1 (x:z) and are discretized to 512 $\times$ 256 grid points, with a constant horizontal grid spacing which gives a resolution of $\approx$ 11 km. The vertical grid spacing is refined towards the rock-air interface, where the resolution reaches 4 km. On average 100 Lagrangian tracers per grid cell are used to track the different compositions included in the model (i.e., the mantle, weak crust, continent and sticky-air) and the physical interfaces (e.g., the free surface) in the subgrid resolution (e.g., Crameri & Tackley, 2015; Crameri & Lithgow-Bertelloni, 2018; Grima et al., 2020).

2.4 Boundary and Initial Conditions

Our top boundary condition is a sticky-air layer after Crameri et al. (2012), which simulates a free surface. Our bottom boundary is free slip and the side boundaries are periodic to prevent unnatural forcing during the model's longer evolution (*c.f.,* Chertova et al., 2012). The top boundary including the sticky-air layer is set to a constant 300 K and the bottom boundary is set to insulating with a zero heat flux condition (Fig. 1).

Parameter	Symbol	Non-dimensional value	Dimensional value	Units
Reference viscosity	η_0	1	$7.74 \cdot 10^{21}$	Pa s
Mantle depth	D	1	2890	km
Upper-mantle depth	D_{UM}	0.23	660	km
Gravitational acceleration	g	-	9.81	ms^{-2}
Thermal conductivity	K	-	3	$Wm^{-1}K^{-1}$
Thermal diffusivity	κ	1	$7.58 \cdot 10^{-7}$	m^2s^{-1}
Thermal expansivity	α	-	$3 \cdot 10^{-5}$	K^{-1}
Temperature difference	ΔT	1	2,500	K
Reference density	ρ_0	1	3,300	kg m^{-3}
Heat capacity	C_{po}	-	1,200	$Jkg^{-1}K^{-1}$
Internal heating rate	H	18.08	$4.92 \cdot 10^{-12}$	Wkg^{-1}
Gas constant	R	-	8.314	$Jmol^{-1}$ K^{-1}
Clapeyron slope$_{660}$	γ_{660}	-	-2.5	$MPaK^{-1}$
Density jump$_{660}$	ρ_{600}	-	341	kg $m^{-}3$
Activation stress	σ_{TS}	-	20	MPa
Plasticity				
Friction coefficient	μ	0.25	-	-
Cohesion	C	1,577	$10 \cdot 10^6$	Pa
Max. yield stress	S	$8.551 \cdot 10^5$	$600 \cdot 10^6$	Pa
Diffusion creep				
Activation energy	E_{*diff}	14.43	300	$kJmol^{-1}$
Activation volume	V_{*diff}	9.0	$2 \cdot 10^{-6}$	m^3mol^{-1}
Dislocation creep				
Activation energy	E_{*disl}	20.7	300	$kJmol^{-1}$
Activation volume	V_{*disl}	4.5	$1 \cdot 10^{-6}$	m^3mol^{-1}
Powerlaw index	n	3.5	-	-
Sticky-air layer				
Thickness	d_{st}	0.05	150	km
Viscosity	η_{st}	$10^{-3}\eta_0$	$7.74 \cdot 10^{18}$	Pa s
C-condition[a]	C_{Stokes}	0.013	-	-
Weak crustal layer				
Thickness	d_{crust}	0.005	15.2	km
Viscosity	η_{crust}	η_0	$7.74 \cdot 10^{21}$	Pa s
Friction coefficient	μ_{crust}	0.001	-	-
Cohesion	C_{crust}	1577	$10 \cdot 10^6$	Pa s
Continent				
Thickness	d_c	0.0721	200	km
Width	W_c	0.712	2000	km
Viscosity	η_c	$100\eta_0$	$7.74 \cdot 10^{24}$	Pa s
Friction coefficient	μ_c	0.5	-	-
Density contrast	$\Delta_{\rho c}$	0.087	-25.0	kg m^{-3}

Table 1. Table of model parameters used in this study. [a] indicates suitable free-surface approximation with sticky-air approach if $C_{stokes} << 1$ (Crameri et al., 2012)

Our initial condition is one of ongoing subduction with a 400 km long slab dipping at 30° (Fig. 1). The slab dip angle is initially defined between 150-250 km depth and is subsequently allowed to evolve freely. Through the model evolution, the shallow slab dip angle is automatically measured at a 175 km depth and the deep slab angle is measured at the slab tip. The slab thickness has an initial constant thickness corresponding to the surface plate thickness at the trench. Our set-up also features a spreading boundary at the edges of the model, which self-consistently evolves into a divergent plate boundary throughout the model evolution (Fig. 1). The initial temperature field describes a standard $\sqrt{age - law}$ to account for a thickening plate from the ridge towards the trench. The initial plate thickness is described by $W_{BL}(x) = W_{BL,0} \cdot \sqrt{\Delta X_{sc}}$, where $W_{BL,0}$ is a constant controlling the maximum thickness of the plate, x is the horizontal coordinate and $\Delta\ X_{sc}$ is the distance from the spreading centre at any given position x. The initial temperature is related to the plate age by $T_z(x) = T_0 \cdot erf[\frac{1-z}{W_{BL}(x)}]$, where $T_0 = 0.64$ and is the initial non-dimensional mantle temperature and z is the vertical coordinate ranging between 0 at the bottom and 1 at the top boundary. The plate's non-dimensional initial thickness is ≈ 0.04D based on previous work which suggests that this is a typical boundary layer thickness for a $Ra = 10^7$ and $H = 18.08$ (Crameri & Tackley, 2015). No weakening is imposed at the ridges at the edges of our model domain and spreading occurs as a natural consequence of the half-space cooling law we implement and the internal dynamics of our model.

2.5 Diagnostics and Model Analysis

We post-process and analyse our model outputs using the geodynamic diagnostic, post-processing and visualisation software StagLab 4.0 (Crameri, 2018) (`https://zenodo.org/record/3596400`), where we quantitatively track (i) the plate velocities at the surface, (ii) the amount of trench retreat, (iii) the shallow and deep slab dip angles, (iv) the evolution of topography, (v) and the slab and mantle properties. Lastly, we qualitatively examine the slab morphology within the upper mantle and at 1000 km depth.

3 Results

3.1 The Role of the Overriding Plate Type and the Lower Mantle Viscosity Increase on Slab Dynamics and trench retreat

We compare the slab dynamics for our reference model V1 with an oceanic and continental overriding plate and find that the presence of continental lithosphere at the trench decreases the trench mobility at the surface and encourages a steeper slab angle at shallow depths in agreement with previous work (e.g., Holt, Becker, & Buffett, 2015). We note that when the overriding plate is continental, the deep slab tip angle is also steeper, resulting in minor slab tip penetration below 660 km. On the contrary, the same slab subducting under an oceanic overriding plate will deflect and flatten above 660 km depth. Comparing the two slab morphologies, we observe that in a continent-ocean subduction, the slab body (i.e., the area of slab between the slab tip and the trench) has undergone significant deformation seen in the slab's undulating and kinked morphology, which is in contrast to the straight slab segment that links the flattened slab toe with the surface in the V1 ocean-ocean case (Fig. 2).

We observe similar slab behaviour when we draw the same comparison for model V2. In this case, the lower mantle viscosity increase occurs at 1000 km depth and the contrast in slab behaviour for different overriding plate types is even more pronounced than what we observe in V1. We note that when the overriding plate is continental, the slab flattens above 660 km depth and simultaneously sinks into the lower mantle below 1000 km, resulting in a "stepped" slab morphology. Similar to the continent case for model V1, the slab body in the V2 case with a continental overriding plate also exhibits an undulating and kinked morphology. Slab behaviour for V2 with an oceanic overriding plate

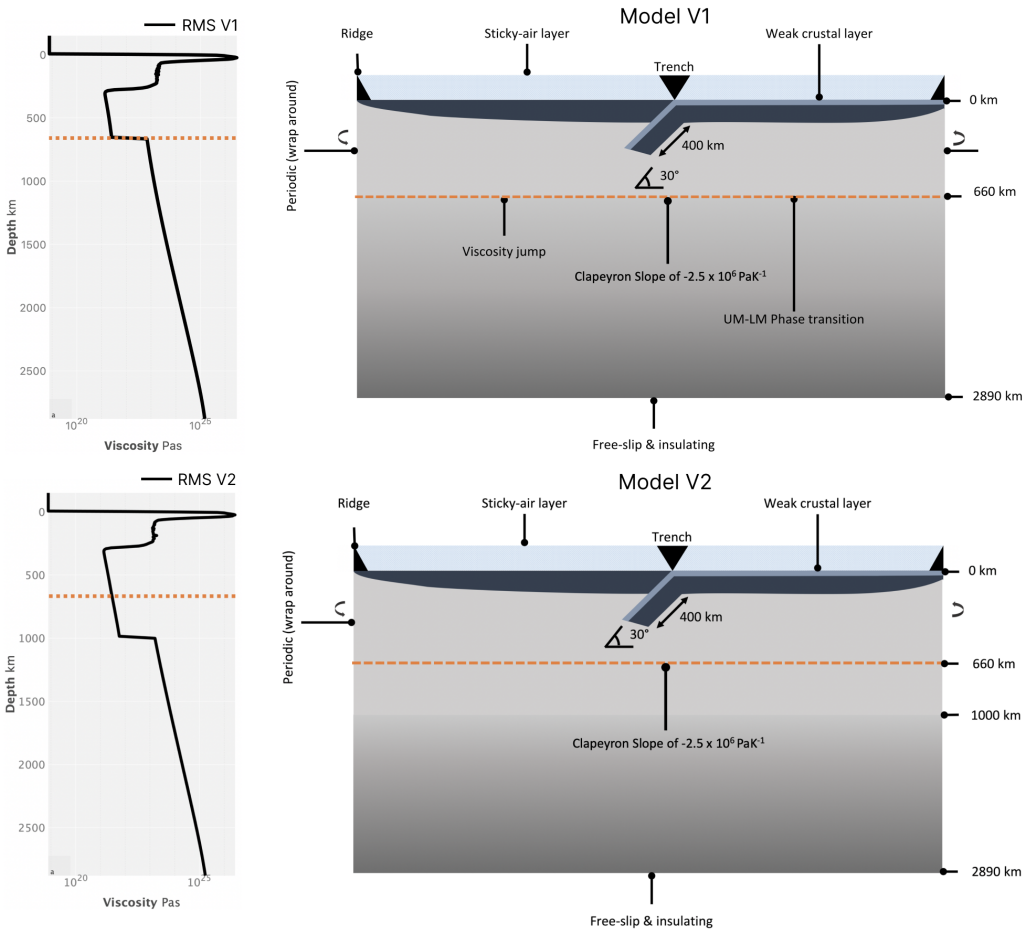

Figure 1. Left: 1D root mean square of the viscosity for V1 and V2 models respectively. **Right:** Cartoon of model setup for reference case V1 and case V2 showing the two spreading ridges on either end of the upper and lower plates, a weak crustal layer overlying the subducting plate, and a sticky-air layer top boundary condition. Darker grey colours indicate the higher viscosity lower mantle. The orange dotted line at 660 km depth delineates the phase transition of ringwoodite to bridgmanite and ferropericlase with a Clapeyron Slope of -2.5 $\cdot$ 10^6PaK^{-1}, for case V1 this also coincides with the lower mantle viscosity increase. For V2 the phase change and the viscosity jump are separate. The initial slab angle is 30 $\circ$ degrees and initial slab length is equal to 400 km. Cartoon setup shows an oceanic overriding plate, this is replaced by thicker, stronger and more buoyant continental lithosphere for V1 and V2 continental cases (see Table 1 for more details).

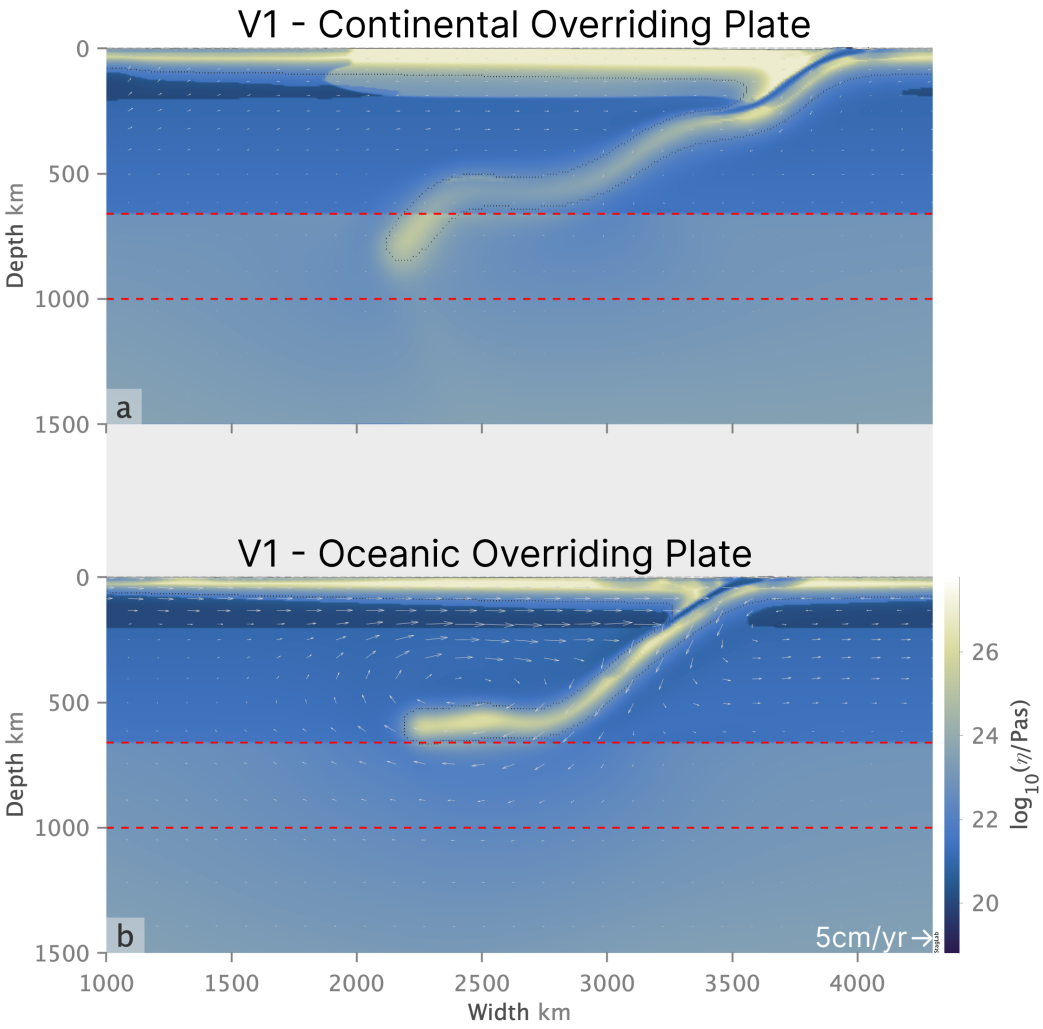

Figure 2. Plots of the viscosity with darker blue shades indicating lower viscosity, for the V1 model with a viscosity increase at 660 km depth, coincident with the bridgmanite phase transition, with continental (a) and oceanic (b) overriding plates. White arrows indicate the magnitude and direction of the induced viscous flow in the models and red dotted lines delineate the 660 km and 1000 km depths. Observe the limited slab tip penetration into the lower mantle for a continental overriding plate (a) vs. slab tip flattening for an oceanic overriding plate, indicating that the overriding plate type can influence the deep slab dynamics

mimics that of V1 with an oceanic overriding plate. In both cases when the overriding plate is oceanic, the slab flattens and deflects at 660 km depth (Fig. 3).

Our results clearly indicate that the combination of the viscosity structure and a continental overriding plate directly influences the slab behaviour at the top of the lower mantle. To investigate this further we plot the trench velocity and the angle of the slab tip (i.e., the deep slab angle) against time for both V1 and V2 cases with a continental overriding plate (Figs. 4 and 5).

We find that for the V1 continental case (Fig. 4) the angle of the slab tip decreases with time indicating a flattening slab toe following an initial slab steepening period during the "slab free fall" stage early in the model evolution (e.g., Funiciello et al., 2003).

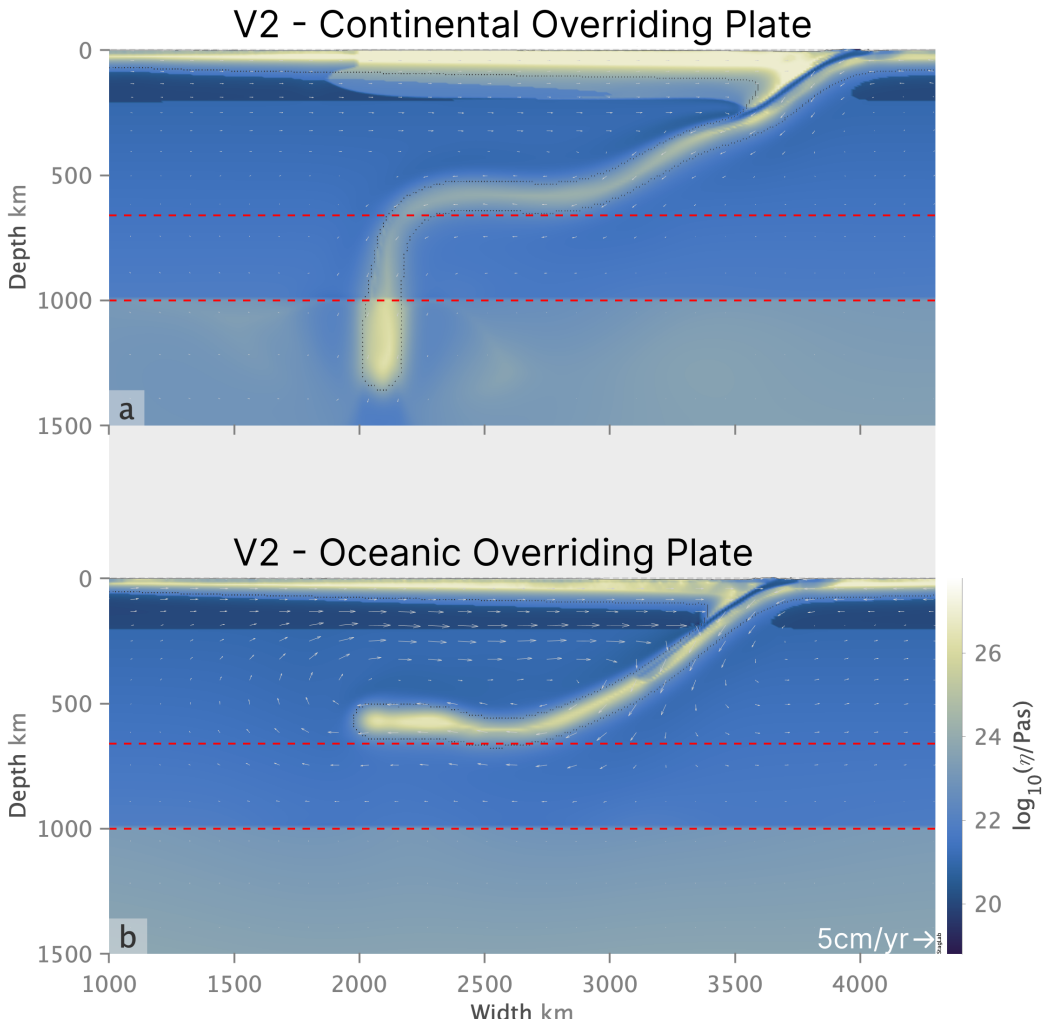

Figure 3. Plots of the viscosity for the V2 model with a viscosity increase at 1000 km depth, separate from the phase change at 660 km depth. Colours and lines as in Fig. 2 above. Note the significant slab tip penetration into the lower mantle for a continental overriding plate (a) vs. slab tip flattening for an oceanic overriding plate, highlighting the combined influence of the continent and the viscosity structure of the mantle in regulating the slab influx from the upper to the lower mantle and dynamics of deep slabs

The slab tip angle increases once again during the later stages of the model evolution indicating a minor steepening. The velocity of the trench also shows a sharp increase early on in the model evolution, with velocities stabilizing to average ~ 1.1 cm year^{-1} between ~ 30 Ma and 70 Ma. During this stage the slab dynamics are dominated by trench rollback and slab flattening above 660 km depth. Trench velocities drop drastically after 80 Ma, reflecting a decrease in rollback.

In case V2 continental (Fig. 5) following the slab free fall stage, the slab tip angle temporarily decreases during a transient period between ~ 10 and 25 Ma when the slab defects and flattens at 660 km depth. Slab tip steepening starts to increase once again after 30 Ma and dominates the rest of the model evolution. Contrary to the trench velocity trend observed for the V1 continental case, in V2 continental, trench velocities show a consistent decrease. The only exception occurs between ~ 10 and 25 Ma during the transient slab flattening period, reflecting an increase in trench rollback.

Figs. 4 and 5 show that when the overriding plate is continental lithosphere, trench velocities and slab dip angles are anti-correlated. As the slab tip angle increases the trench velocity increases and vice-versa. This trend is particularly clear throughout the lifetime of the V2 continental case and during the initial and middle age stages for the V1 continental case. However, when the overriding plate is oceanic the trench velocities and the slab dip angles are correlated, with drops in trench retreat velocities also corresponding to drops in deep slab tip steepness (Figs. A2 and A3).

Comparing the trench velocities across models with and without a continental overriding plate for both V1 and V2 cases, we also find that surface plate velocities are reduced when the overriding plate is continental (see Figs. 4 and 5 vs. A2 and A3) in agreement with previous work (e.g., Butterworth et al., 2012; Sharples et al., 2014; Holt, Buffett, & Becker, 2015). The faster plate motions for the ocean-ocean cases favour slab rollback in the upper mantle and encourage slab deflection at 660 km depth.

3.2 The Slab Dip Ratio and Slab Stages

To quantitatively compare the slab evolution at the top of the lower mantle, we define a slab bending ratio S_b. We calculate S_b by dividing the deep slab tip angle by its shallow counterpart at ~ 72 km depth. S_b provides a measure of the overall steepness of the slab as opposed to just an indication of the slap tip dip. The S_b ratio is a reflection of the slab's deformation and sinking history and is therefore a useful lens through which one can understand the slab evolution as this sinks from the shallow upper mantle towards the top of the lower mantle.

When S_b is > 1, the subducting slab is characterised by a steep slab morphology, fast vertical slab sinking velocities and rapid penetration through the upper mantle (Fig. 6a). We term this stage the "vertical sinking stage" and it is comparable to the slab free-fall stage described in Funiciello et al. (2003). The slab's initial vertical sinking stage is followed by a "deformation stage" (Fig. 6b), where its S_b values become equal to around 1. In this stage, the vertical sinking of the slab tip deeper into the mantle is reduced, trench retreat increases and the slab undergoes significant intra-slab bending as it adjusts from a steep to a deflected morphology. When the overriding plate is oceanic and/or the mantle viscosity jump occurs at 660 km depth, the slab enters its "flattened stage" which is defined by an S_b ratio < 1 (Fig. 6c). Small S_b values indicate that the now deflected slab has limited lower mantle penetration. Deflection can result in either a flattened slab underlying the overriding plate at depth or a "hooked" slab morphology (see Appendix Appendix A, section A3 and Fig. 6c) that bends underneath the subducting plate, away from the overriding plate. Subduction is now dominated by trench rollback, which drags the slab through the upper mantle. When the overriding plate is continental lithosphere, the "deflection stage" is followed by a "renewal stage" (Fig. 6d). This stage is marked by S_b values higher than 1, and reflects a renewed period of slab tip steep-

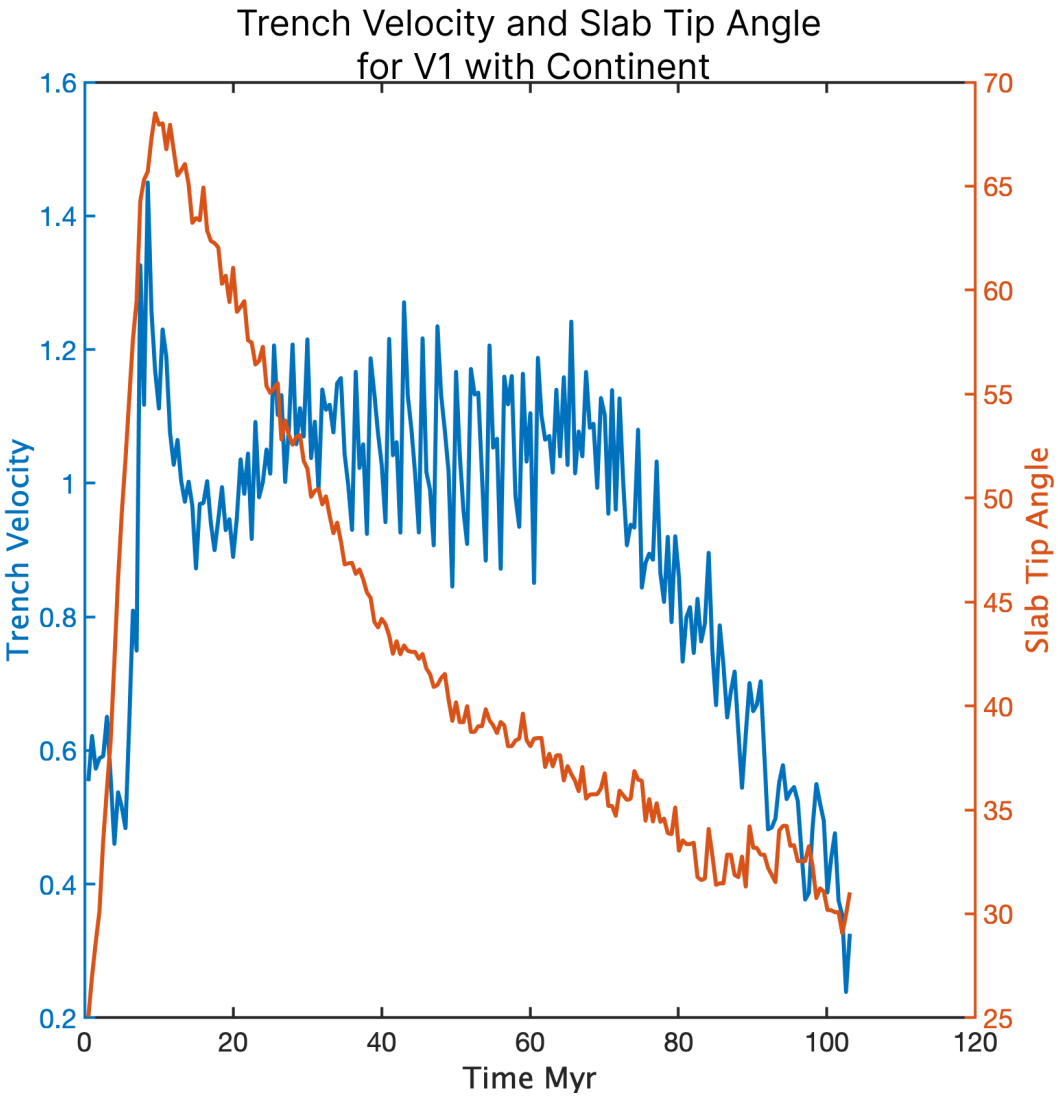

Figure 4. Graph of trench velocities in cm year $^{-1}$ on the left in blue and slab dip angles in degrees on the right in orange for a continental overriding plate type for viscosity profile V1. Slab dip angles show a consistent downward trend throughout the model evolution indicating slab flattening. The trench velocity is constant for most of the model evolution bookended by rapid trench rollback at the start of the model and significant decrease at the end.

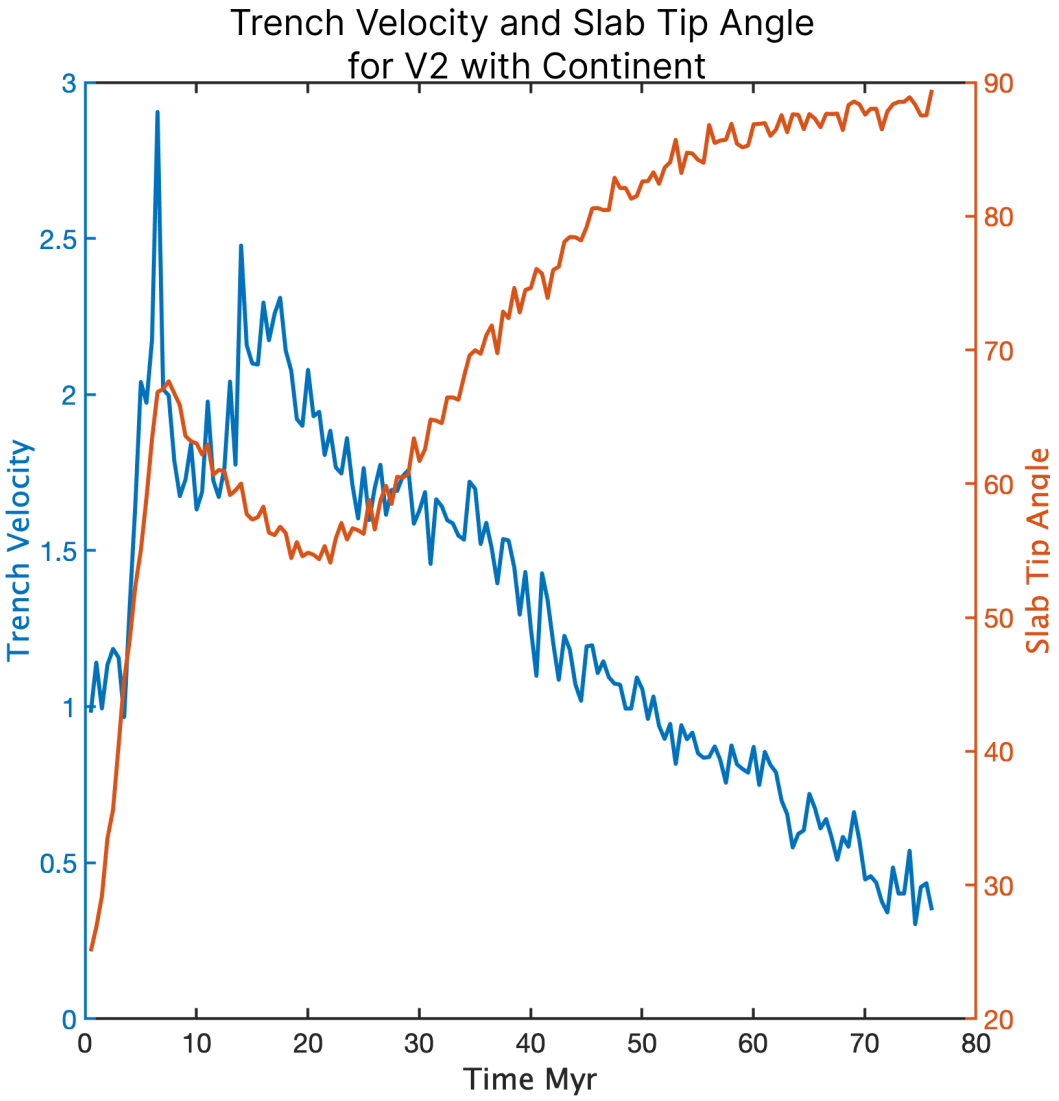

Figure 5. Colours and lines as in Fig. 4. Trench velocities and slab dip angles for a continental overriding plate type for viscosity profile V2. In V2 the model is dominated by significant slab steepening shown here by the increases in the deep slab dip angles and a drop in the trench mobility shown by the decrease in trench velocity.

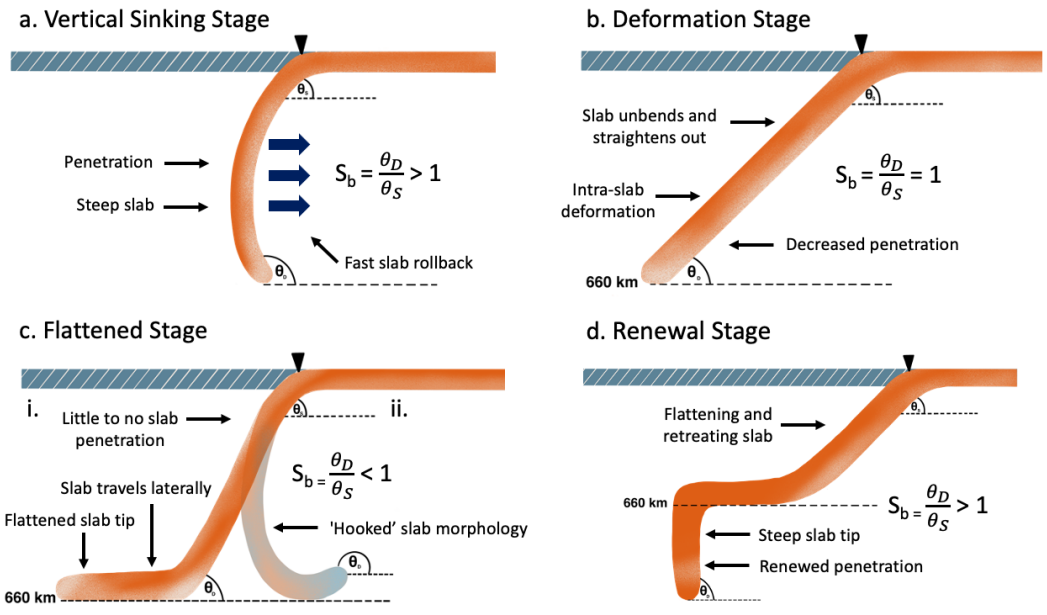

Figure 6. Schematic of the slab bending ratio S_b with the overriding plate shown in blue and the subducting plate shown in orange. The S_b ratio describes the slab bending and is calculated by dividing the deep slab dip angle by the shallow slab angle at the trench. An S_b ratio higher than 1 indicates a slab in its initial vertical sinking stage (a), characterised by fast penetration through the upper mantle, slab rollback and steep slab dip angles. S_b equal to 1 indicates a slab undergoing significant intra-slab deformation, limited vertical penetration through the mantle and increased trench rollback (b). S_b less than 1 is representative of a slab that is in its flattened stage, with little to no vertical penetration into the lower mantle below it and significant lateral motion of the flattened slab (c). When the overriding plate is continental renewed slab tip steepening produces higher S_b ratios and renewed vertical sinking and penetration at the top of the lower mantle (d).

ening and renewed vertical slab sinking velocities. Lower mantle penetration is maintained through the steep slab tip, which drags the slab to deeper depths. This lower mantle pull is however offset by the slab deflection in the upper mantle which arises from the resistance to subduction from the bridgmanite phase transition at 660 km depth and the induced viscous flow from the trench-ward motion of the continental overriding plate. The interplay between the slab deflection at 660 km depth and vertical slab tip penetration below 660 km depth results in a stepped slab morphology observed for both V1 and V2 continental cases.

4 Discussion

4.1 The Continental Overriding Plate, The Slab Bending Ratio and Slab Behaviour at the Top of the Lower Mantle

In agreement with previous work (e.g., Sharples et al., 2014; Holt, Buffett, & Becker, 2015; Crameri & Lithgow-Bertelloni, 2018), our results show that the thickness of the

overriding plate controls to some extent the slab dynamics at the bottom of the mantle transition zone. We also note that the strength and density and hence, buoyancy of the overriding plate play an important role in the deep slab dynamics. We show that when the overriding plate is a thin, dense oceanic plate, the subducting slab goes through three distinct stages: a) a vertical sinking stage, b) a deformation stage and c) a flattened stage as its S_b ratio evolves from > 1, $= 1$ and < 1, with the slab ultimately flattening at 660 km depth irrespective of the depth at which the viscosity jump occurs (Fig. 8).

However, when the overriding plate is thick and buoyant continental lithosphere, the viscosity structure of the mantle plays a significant role in determining the slab dynamics at the top of the lower mantle. For these cases, the flattened stage observed in models with an oceanic overriding plate is either followed (in case V1 continent) or replaced entirely (in case V2 continent) by a renewal stage depending on the lower mantle viscosity structure. Comparing the slab behaviour across V1 and V2 with continental overriding plates, we find that the subducting slab has a steeper subduction angle at the trench for both cases. However, the slab tip angle decreases progressively in the V1 case as the slab tip sinks deeper into the mantle (Fig. 4). This overall trend dominates the slab behaviour for the V1 model despite limited slab tip penetration below 660 km depth. In contrast, the slab tip angle in the V2 continental case increases with depth. This behaviour is also reflected in an S_b ratio value, which remains above 1 throughout model evolution, indicating an overall slab steepening behaviour. In this model, the slab exhibits an extended renewal stage with a well developed slab tip below 1000 km depth and a contracted, almost negligible, deflection stage. This is because in V2 continental, slab deflection at 660 km depth (due to both the endothermic phase transition of bridgmanite and the horizontal drag induced by the continental drag as this moves towards the trench) is offset by the deep slab tip pull as the slab tip sinks into the lower mantle during the slab's renewal stage (Fig. 8).

Our results clearly show that when the increase in viscosity occurs at 660 km depth in V1 continent case, slab penetration and interaction with the lower mantle is limited and the amount of slab tip that is involved in the renewal stage is small. When the viscosity jump occurs at 1000 km depth in V2 continent case, the slab's renewal period is extended, leading to a pronounced steep slab tip below 1000 km depth. In the latter case, the steep tip sinks vertically downwards inducing a strong vertical viscous flow, which helps to drag the remainder of the slab above 660 km depth down into the lower mantle with it (Figs. 7 and 8).The dragging motion of the sinking slab tip in V2 is offset by the slab deflection above 660 km depth. The latter is due to the strong basal drag of the continent as this moves towards the trench. Due to the thickness of the continental roots the continent shears and drags the upper mantle towards the trench and induces a strong horizontal viscous flow in the upper mantle. This encourages the slab above 660 km depth to rollback, bend, and deflect (Fig. 7). Slab flattening at 660 km is further encouraged by the phase transition of ringwoodite to bridgmanite and ferropericlase. The delayed endothermic phase transition within the cold slab core introduces an anomalous buoyancy to the slab, which resists subduction (Fig. A1).

Our results clearly show that the slab morphology reflects the interplay between the continental and slab drag forces in the upper and top of the lower mantle, respectively. This force balance between the two is modulated by the viscosity structure of the upper lower mantle. In V2 continent case, the slab deflects due to the presence of the continental overriding plate and the anomalous buoyancy associated with the phase change at 660 km depth, which is offset by the increased slab sinking force between 660 and 1000 km depth, leading to a stepped slab morphology. In V1, the combined viscosity jump and bridgmanite phase transition at 660 km depth resists the slab's sinking at the top of the lower mantle. This, combined with the strong continental drag of the upper mantle towards the trench and limited slab tip penetration below 660 km depth, favours slab deflection above 660 km over slab sinking for the V1 continental case.

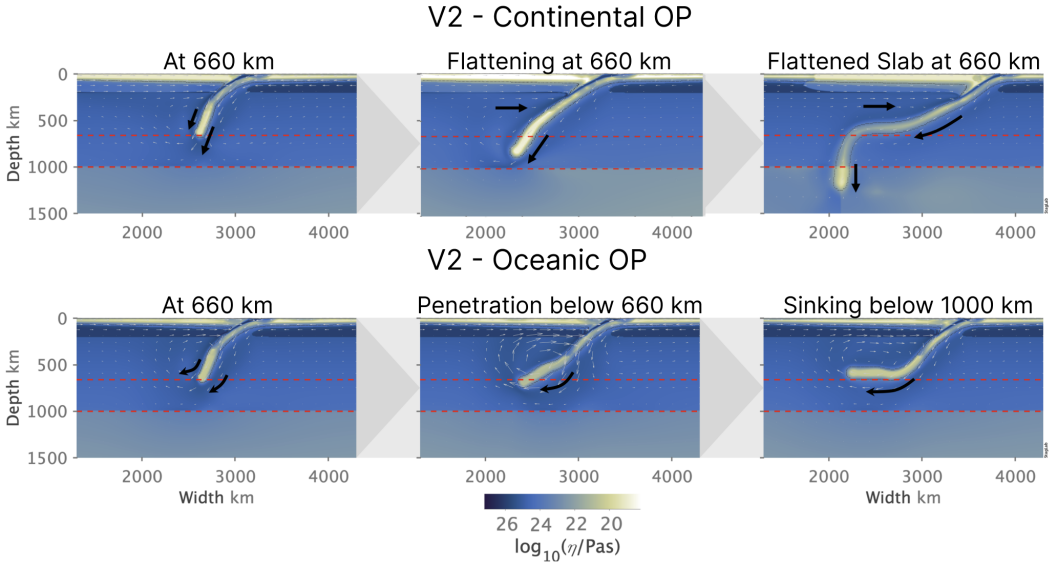

Figure 7. Colours, lines and arrows as in Fig. 2, thick black arrows emphasise the direction of the induced viscous flow. Note the role of the induced predominantly vertical viscous flow on the slab morphology for V2 with a continental overriding plate (top)and the predominantly horizontal flow in an ocean-ocean setting (bottom). **Top:** The continental overriding plate drags the shallow upper mantle towards the slab encouraging slab rollback in the upper mantle. The vertical flow induced by the steeply sinking slab tip drags the subducting slab below 1000 km depth. This results in a stepped slab shape. **Bottom:** The thinner oceanic overriding plate results in shallow slab dip angles and encourages faster overall surface plate motions resulting in strong horizontal viscous flow in the upper mantle, trench rollback and slab flattening above 660 km depth.

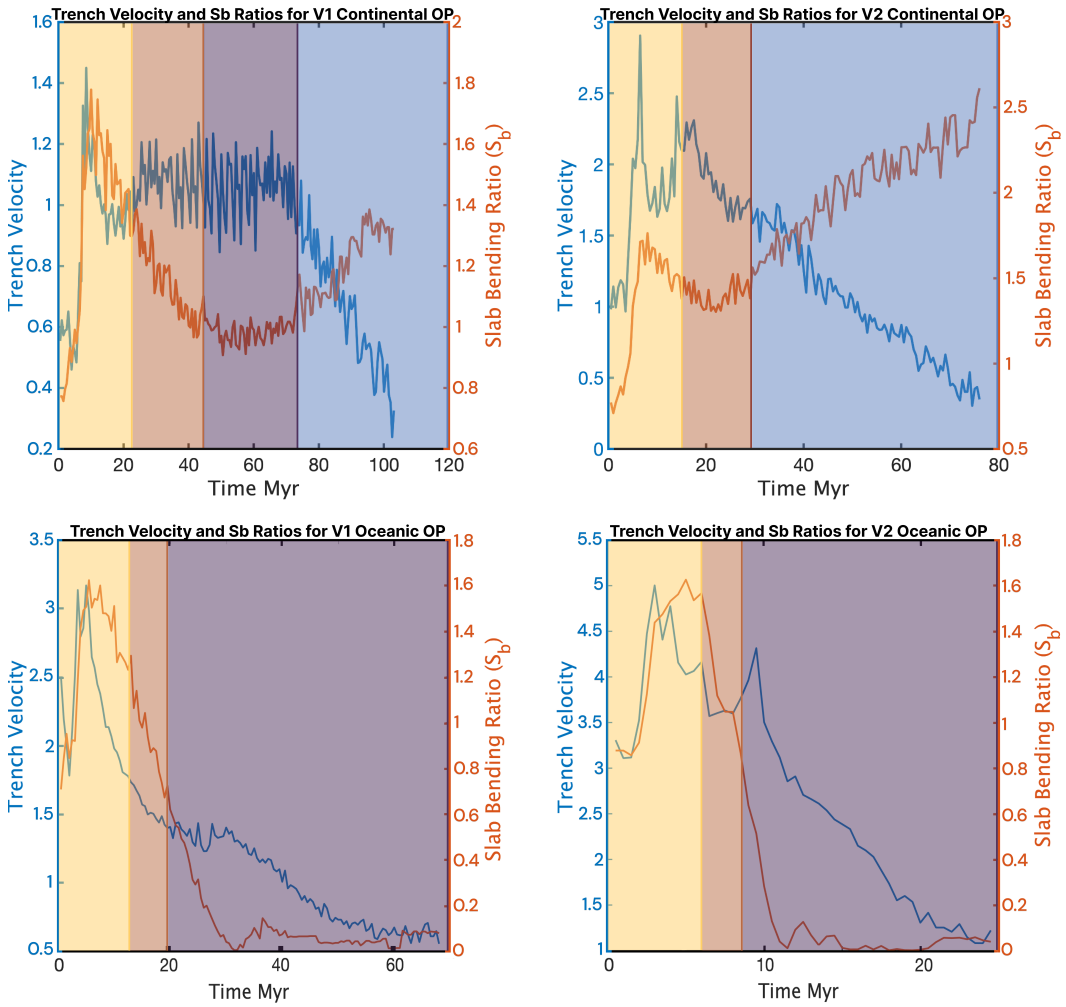

Figure 8. Colours and lines as in Fig. 4 with trench velocity in cm_{yr} in blue and slab bending ratio (S_b) in orange for model V1 with a continental (top left) and oceanic overriding plate (bottom left) and model V2 with a continental (top right) and oceanic (bottom right) overriding plate. The slab's stages are denoted in yellow, orange, purple and blue representing; a. the initial vertical sinking stage, b. the deformation stage, c. the flattened stage and d. the renewal stage respectively. Note the increase in S_b ratios for V1 and V2 continental in the later model stages following decreases in S_b ratios to < 1 and $= 1$ in the middle stages of the model evolution, indicating a renewed period of steepening and increased vertical slab penetration into the lower mantle for both cases. Note also how S_b ratios for the continental cases are anti-correlated with trench retreat values, a trend which is overturned for both V1 and V2 cases with an oceanic overriding plate.

4.2 Analogues in nature

Seismic tomography models show that a plethora of slab morphologies exists between 410 km and 1500 km depth (e.g., Fukao et al., 2009; Fukao & Obayashi, 2013; Goes et al., 2017). Various attempts have been made to explain this diversity in slab shape and various mechanisms have been proposed to this effect including the slab age, the age and thickness of the overriding plate and changes in the effective Clapeyron Slope due to slab dehydration (e.g., Billen, 2008; Garel et al., 2014; Holt, Buffett, & Becker, 2015; Agrusta et al., 2017; Goes et al., 2017). We suggest that some of this heterogeneity in slab morphology might also be due to the induced viscous flow in the upper mantle and top of the lower mantle modulated by the type of overriding plate, the phase transition of bridgmanite, and the depth of the lower mantle viscosity increase.

We suggest that the stepped slab morphology observed under the South Peruvian continental arc observed in both UU-P07 and TX2019slab seismic tomography models (Amaru, 2007; Lu et al., 2019) reflects the combined effects of continental drag towards the slab in the upper mantle and the resistance provided by the anomalous buoyancy of the untransformed bridgmanite within the slab core. The resulting effect is slab deflection above 660 km depth, which is mitigated by the pull of the steep slab tip as this sinks into the lower mantle during the slab's renewal stage when its S_b ratios increase above 1 (Fig. 9). Meanwhile, slab flattening and deflection above 660 km depth without any further sinking to deeper depths is observed for the ocean-ocean subduction at the Izu-Bonin arc. In this case, the higher plate mobility typical for ocean-ocean systems results in higher values of slab rollback in the upper mantle resulting into slab deflection at the bottom of the mantle transition zone (Fig. 9).

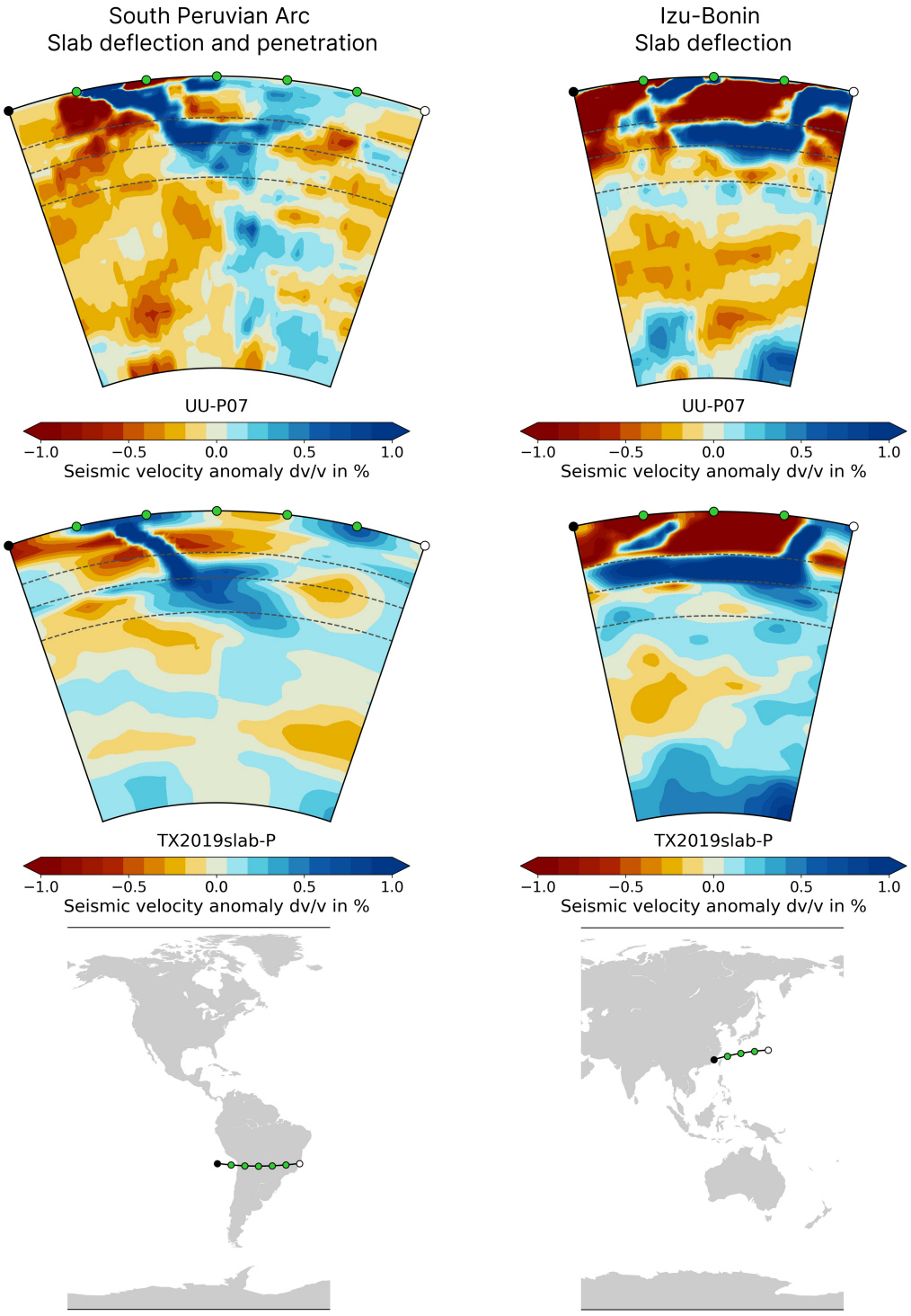

Figure 9. Seismic tomography cross-sections from the portal SubMachine (`http://www.earth.ox.ac.uk/~smachine/cgi/index.php`) (Hosseini et al., 2018) using model UU-P07 (Amaru, 2007) (top) and model TX2019slab (Lu et al., 2019) (bottom). Warm colours indicate slower than average P-wave velocities and cooler colours show faster than average P-wave velocities. Both seismic tomography models show a stepped slab morphology indicating slab deflection above 660 km depth complementary with slab tip penetration below 1000 km depth for the Nazca slab subduction underneath the Southern Peruvian continental arc (left) and slab flattening above 660 km depth for the Izu-Bonin subduction zone (right).

4.3 Model Limitations

Our results show that the deep slab morphology is strongly controlled by the interplay between the overriding plate type and the viscosity structure of the top of the lower mantle. However, in nature, the strength of the subducting slab is expected to be controlled by a range of factors, including evolving grain size, and other damage memory (e.g. Montési, 2013; Bercovici & Ricard, 2016; Dannberg et al., 2017; Heilman & Becker, 2022). The implications of these contributions on the effective viscosity and yield stress are only approximately represented by our relatively simple rheological setup. The rheology of our models is also simplified by excluding a multi-mineralic slab and mantle and the effect of slab dehydration on the dynamics. These simplifications may have important implications for the slab behaviour and slab induced viscous flow.

Moreover, mantle flow in nature is, of course, 3-D and due to the restriction of our simplified models, we thus, miss the toroidal flow component. The latter may play a significant role in slab rollback and slab penetration into the lower mantle (e.g., Stegman et al., 2006; Faccenna & Becker, 2010; Capitanio & Replumaz, 2013).

We adopt this simplified approach to isolate the effects of the relationship between the overriding plate and the mantle viscosity structure on the deep slab dynamics. While the temporal evolution of the slab morphology and the timing of the slab's penetration into the lower mantle may be affected by all of these complexities, we expect the relative effects of the overriding plate and the viscosity structure on slab dynamics to be fairly similar.

5 Conclusions

We find that the nature of the overriding plate plays a controlling role on deep slab dynamics and directly influences the slab's bending ratio S_b. This ratio describes the amount of bending and vertical sinking experienced by the slab and is measured by dividing the deep slab angle by the shallow slab angle at the trench. Modelled slabs subducting underneath an oceanic overriding plate exhibit S_b ratios smaller than 1 and will deflect and flatten at 660 km depth irrespective of the mantle viscosity structure. This indicates that for ocean-ocean convergence such as that observed at the Izu-Bonin subduction zone, deep slab dynamics are mostly controlled by the trench rollback at the surface and the temperature dependence of the phase boundary depth of the ringwoodite to bridgmanite and ferropericlase (see sec. A1 and Fig. A1 b)

However, when the overriding plate is continental, the viscosity structure of the mantle has a stronger control on the slab dynamics. We show that with a lower mantle viscosity increase at 660 km depth and a continental overriding plate, the S_b ratio values register a second increase above 1 later in the model stages reflecting a renewal stage with limited slab tip steepening and vertical sinking below 660 km depth. However, in this case, both the slab tip steepening and its renewed lower mantle sinking are curtailed due to the higher viscosity of the lower mantle. On the other hand, the combined effect of continental lithosphere and a viscosity jump at 1000 km depth encourages and prolongs the slab's renewal stage. In this case, the slab's S_b ratio value remains above 1, resulting in the slab tip steepening and the further vertical sinking of the slab tip deeper into the lower mantle. This behaviour is further encouraged by the induced vertical viscous flow at the top of the lower mantle, which drags the slab tip vertically downwards. The prolonged renewal stage for models with a deeper viscosity increase and a continental overriding plate offsets the slab deflection effects in the upper mantle stemming from the continental drag and the effects of the bridgmanite forming reactions. This interplay between forces in the upper mantle and at the top of the lower mantle produces a stepped slab morphology observed in the Nazca slab as it subducts underneath the Southern Peruvian continental arc.

Our study underscores the importance of investigating deep slab dynamics in a more complete framework that includes a buoyant, strong continental lithosphere and a mantle viscosity structure beyond that of a simple increase at 660 km depth. We show that the slab morphology at depth is an expression of the overriding plate type, the induced flow in the mantle and the mineral physics; and is largely modulated by the viscosity structure of the mantle transition zone and the top of the lower mantle.

Acknowledgments

AGG was supported by the Commonwealth Scholarship Commission and the Slichter endowed chair to CL-B, and FC was supported by the Research Council of Norway Centers of Excellence (223272). Computations were performed on the UK NERC funded supercomputer *Archer* (NE/M00046X/1). The authors thank Paul Tackley for providing the code STAGYY.

6 Data Availability

The data generated for this study, the StagYY input parameter files used and the Matlab code used to generate and plot the trench velocities and the S_b ratio used in this study are publicly available on this repository; `https://zenodo.org/records/10655407`. The geodynamic diagnostic, post-processing and visualisation software StagLab 4.0 used in this study is available from `https://zenodo.org/record/3596400` and the code finite difference code StagYY is available upon request.

Appendix A

A1 The Combined Effect of The Plate Type and the Ringwoodite to Bridgmanite and Ferropericlase Phase Transition

As discussed briefly in sec. 4 above, the temperature dependence of the phase boundary depth of the ringwoodite to bridgmanite and ferropericlase encourages the formation of a lens of low density, untransformed material within the cold slab core at 660 km depth (Fig. A1). This lends to the slab an anomalous buoyancy at 660 km depth, which resits the slab's further sinking into the lower mantle. For case V2 oceanic, this anomalous buoyancy reinforces the slab's flattening and deflection arising from the pronounced slab rollback due to the increased mobility of the surface plates (Fig.A1).

A2 Trench Velocities and Slab Tip Angles for V1 and V2 with an Oceanic Overriding Plate

Plots of the trench velocity against deep slab dip angle for ocean-ocean subduction for models V1 and V2 showing a correlation between the trench velocity and the deep slab tip, with slab tip angles decreasing as trench velocity values drop (Figs. 4 and 5). We note that in both V1 and V2 oceanic overriding plate cases, this relationship between trench velocity and slab tip angle produces slab flattening and deflection above 660 km depth (Figs. 2 and 3).

A3 The Effect of A Low Viscosity Layer at the Top of the Lower Mantle

Following the work of Rudolph et al. (2015, 2020), which suggests the presence of a low viscosity layer (LVL) at the top of the lower mantle, we also test an additional case V3 with an LVL between 660 and 1000 km depth. To isolate the effects of the LVL, in case V3 we exclude the effects of the ringwoodite phase transition at 660 km depth. Sim-

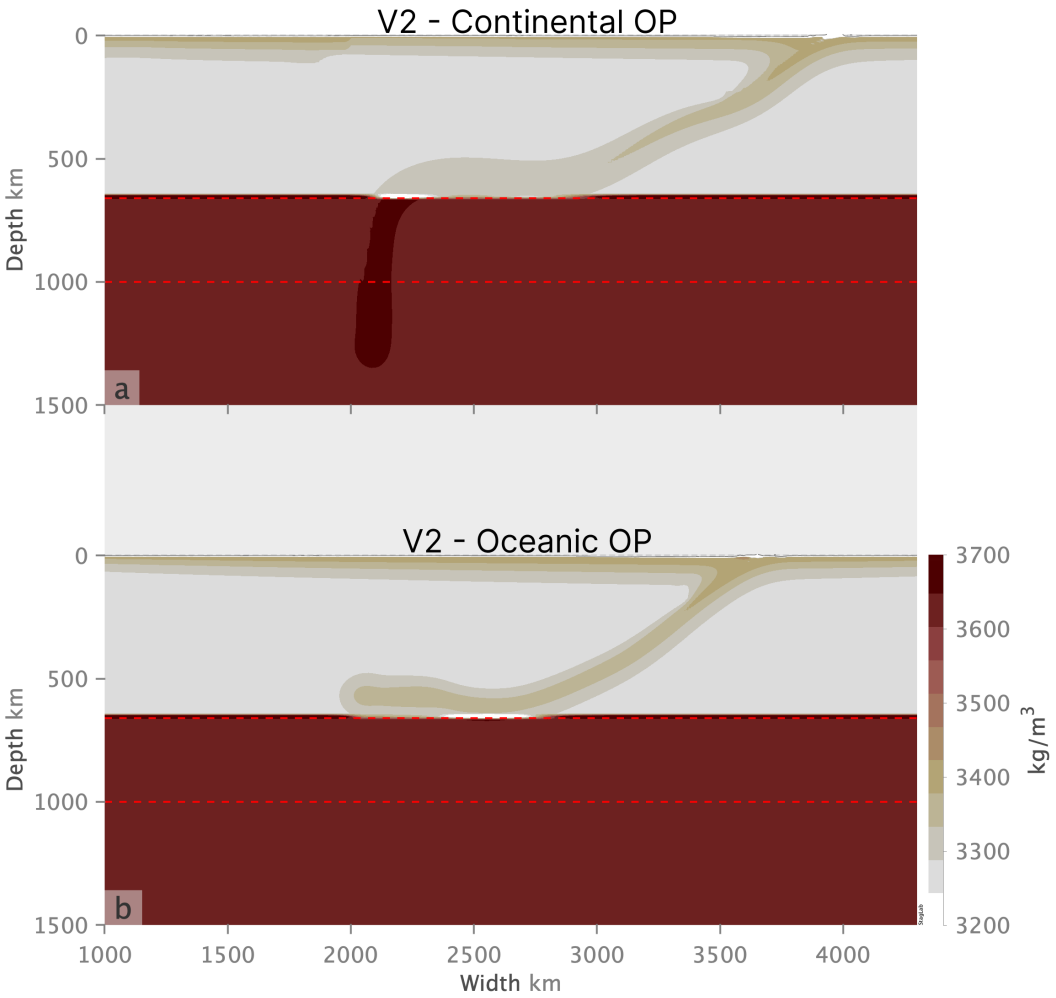

Figure A1. Plot of density illustrating a lens of lower density within the slab core at 660 km depth for V2 with a continental overriding plate (a) and an oceanic overriding plate (b). The low density material resists the subduction of material below 660 km depth. However in (a), this is offset by the pull of vertical slab below 660 km depth once the slab enters its renewal stage. For ocean-ocean subduction (b) the low density lens is wider and more effective at resisting the slab sinking into the lower mantle. In (b), there is no slab pull to offset the resistance to subduction and the slab flattens.

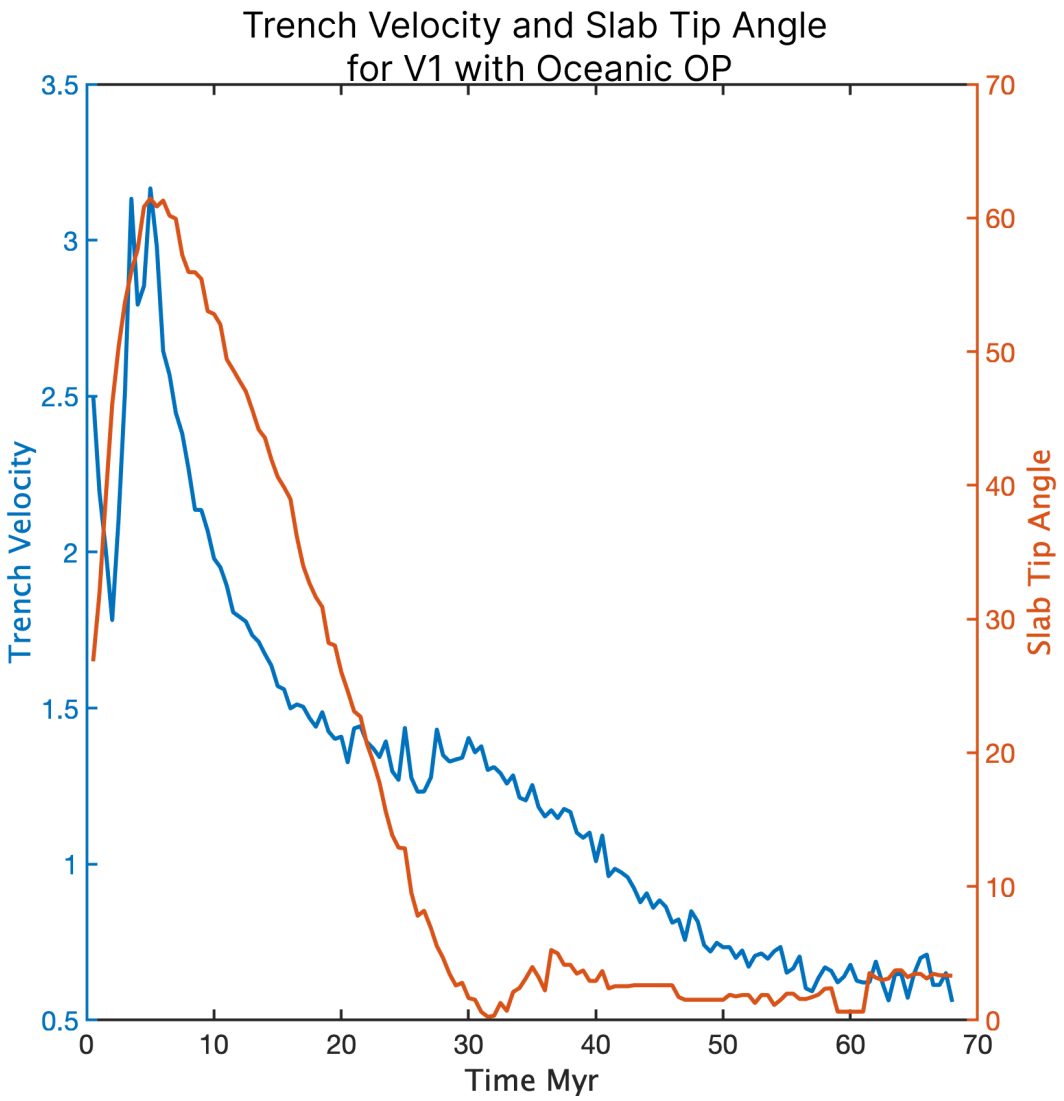

Figure A2. Colours and lines as in Fig. 4. Trench velocities in cm year $^{-}1$ (blue) and slab dip angles in ∘ (orange) for an oceanic overriding plate type for viscosity profile V1. Slab dip angles and trench retreat velocities show a correlation where both register a decrease throughout the model evolution.

ilar to our approach for V1 and V2 cases, we also run our V3 models with an oceanic and a continental overriding plate.

We find that for V3, the slab tip sinks directly into the lower mantle irrespective of the overriding plate type. We attribute this to the presence of the low viscosity layer together with the missing resistance to subduction from the endothermic phase transition, both of which encourage deep slab sinking.

However, we note that despite the overall similar slab behaviour for V3 continental and V3 oceanic, when the overriding plate is strong and buoyant continental lithosphere, the slab morphology takes on a hooked, concave morphology (Fig. A4a). Conversely, when the overriding plate is comprised of the thinner and denser oceanic lithosphere, the slab morphology has a more convex shape (Fig. A4b). This difference in slab

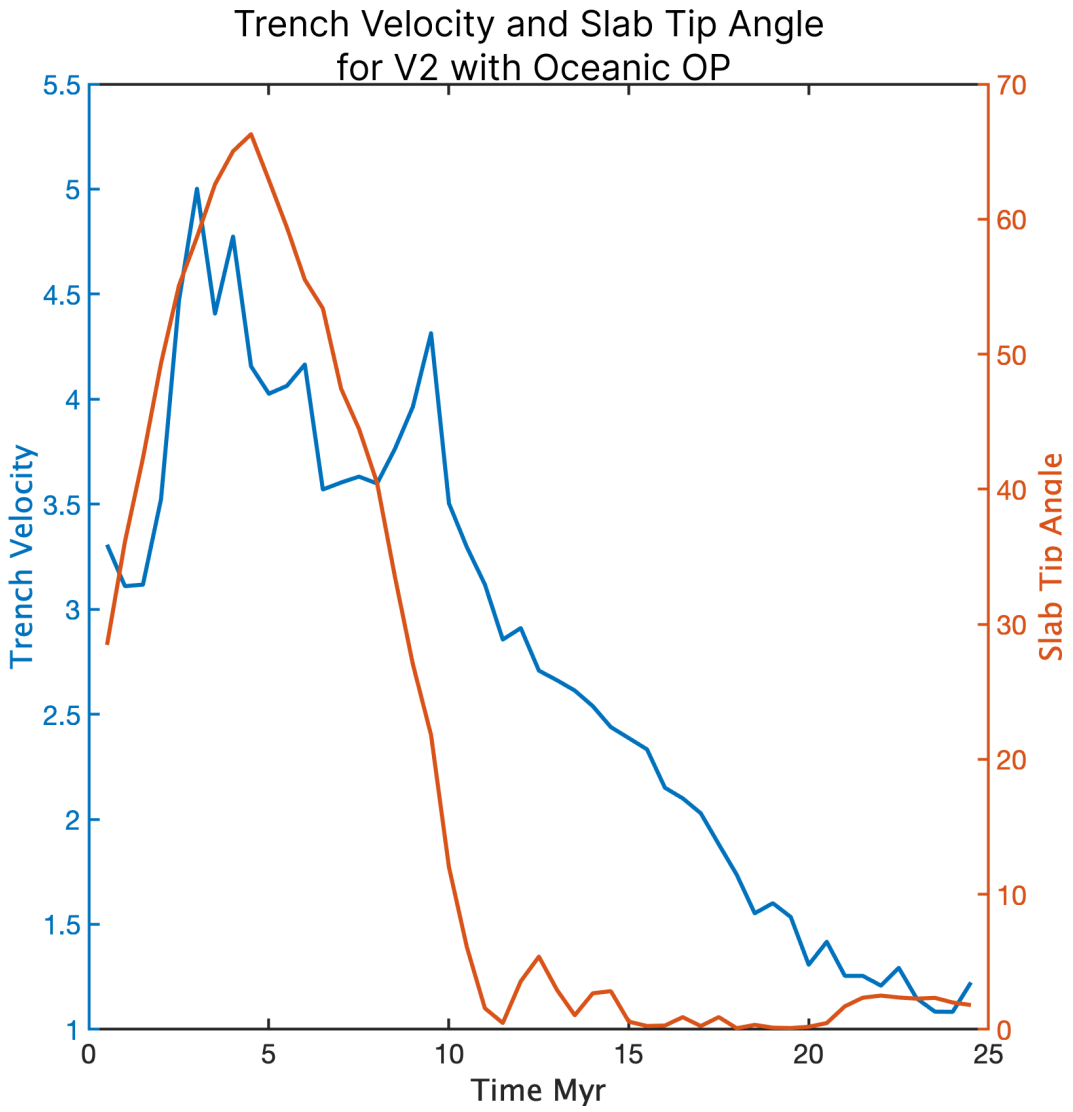

Figure A3. Colours and lines as in Fig. 4. Trench velocities in cm year $^{-1}$ (blue) and slab dip angles in ∘ (orange) for an oceanic overriding plate type for viscosity profile V2. V2 slab dip angles and trench retreat velocities also register a decrease throughout the model evolution, mimicking the correlation observed in Fig. A2.

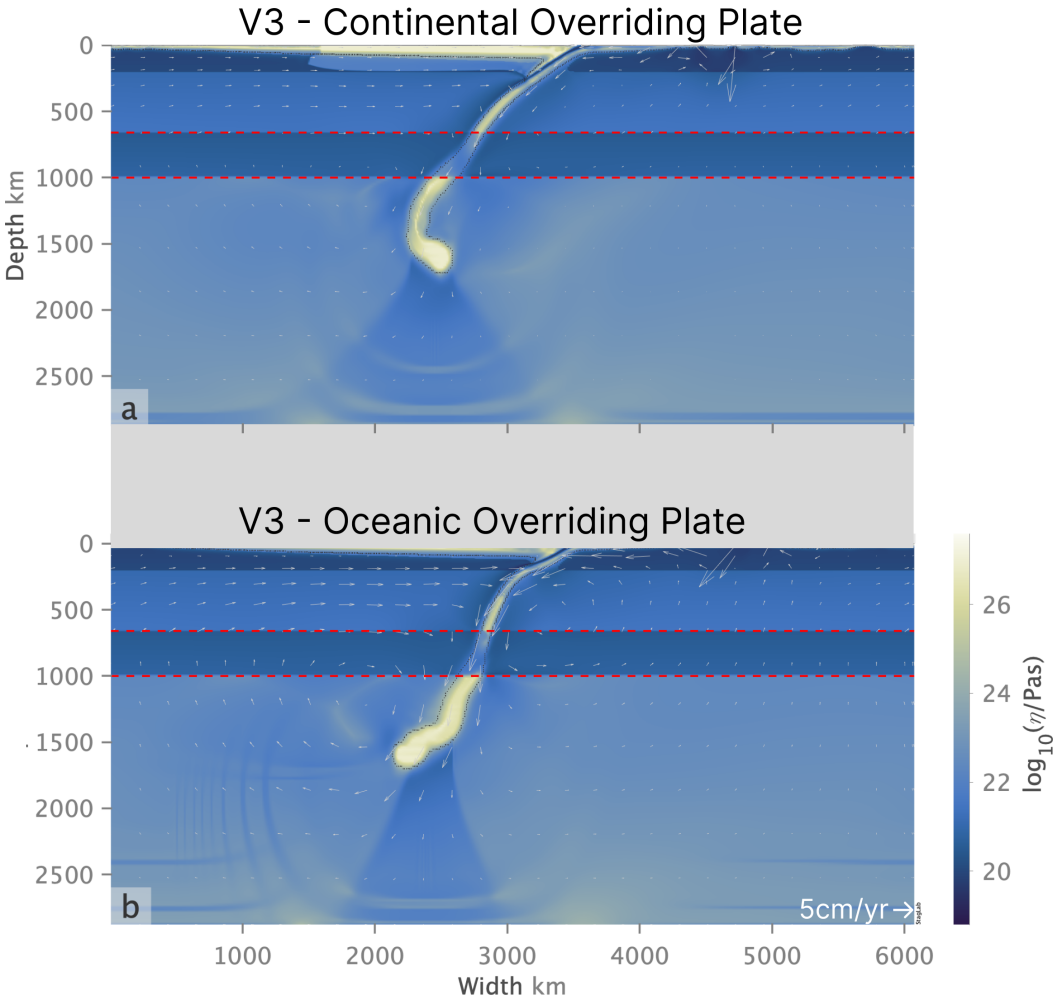

Figure A4. Plots of the viscosity for the V3 model with a viscosity increase at 1000 km depth, no the phase change at 660 km depth and a low viscosity layer between 660-1000 km depth. Colours and lines as in Fig. 2 above. Note the significant difference in slab tip morphology for a continental overriding plate (a) and an oceanic overriding plate, highlighting the steepening effect of the continent on the slab in the upper mantle.

tip shape is the result of the slab angle at the trench. As discussed above, the presence of a continental overriding plate encourages steeper subduction angles at the trench and a reduction in the overall plate mobility at the surface. However, in an ocean-ocean setting the higher slab rollback, encourages comparatively flatter slab morphologies in the upper mantle resulting in a flatter slab tip and a convex slab shape.

References

Agrusta, R., Goes, S., & Hunen, J. V. (2017). Subducting-slab transition-zone interaction : stagnation , penetration and mode switches. *Earth and Planetary Science Letters*, *464*, 10-23.

Amaru, M. (2007). Global travel time tomography with 3-d reference models.

Bercovici, D., & Ricard, Y. (2016). Grain-damage hysteresis and plate tectonic states. *Phys. Earth Planet. Int.*, *253*, 31–47.

Billen, M. I. (2008, may). Modeling the Dynamics of Subducting Slabs. *Annu. Rev. Earth Planet. Sci.*, *36*(1), 325–356. Retrieved from `https://www.annualreviews.org/doi/10.1146/annurev.earth.36.031207.124129` doi: 10.1146/annurev.earth.36.031207.124129

Billen, M. I., & Hirth, G. (2007, aug). Rheologic controls on slab dynamics. *Geochemistry, Geophys. Geosystems*, *8*(8), n/a–n/a. Retrieved from `http://doi.wiley.com/10.1029/2007GC001597` doi: 10.1029/2007GC001597

Butterworth, N. P., Quevedo, L., Morra, G., & Müller, R. D. (2012, 10). Influence of overriding plate geometry and rheology on subduction. *Geochemistry, Geophysics, Geosystems*, *13*, n/a-n/a. Retrieved from `http://doi.wiley.com/10.1029/2011GC003968` doi: 10.1029/2011GC003968

Capitanio, F. A., & Replumaz, A. (2013). Subduction and slab breakoff controls on Asian indentation tectonics and Himalayan western syntaxis formation. *Geochem., Geophys., Geosys.*, *14*, 3515–3531.

Chertova, M. V., Geenen, T., Berg, A. V. D., & Spakman, W. (2012). Using open sidewalls for modelling self-consistent lithosphere subduction dynamics. *Solid Earth*, *3*(2), 313–326. doi: 10.5194/se-3-313-2012

Christensen, U. R., & Yuen, D. A. (1985). Layered Convection Induced by Phase Transitions. *JGR*, *90*.

Conrad, C. P., & Lithgow-Bertelloni, C. (2006). Influence of continental roots and asthenosphere on plate-mantle coupling. *Geophysical Research Letters*, *33*, L05312. Retrieved from `http://doi.wiley.com/10.1029/2005GL025621` doi: 10.1029/2005GL025621

Crameri, F. (2018, jun). Geodynamic diagnostics, scientific visualisation and StagLab 3.0. *Geosci. Model Dev.*, *11*(6), 2541–2562. Retrieved from `https://gmd.copernicus.org/ARTICLEs/11/2541/2018/` doi: 10.5194/gmd-11-2541-2018

Crameri, F., & Lithgow-Bertelloni, C. (2018). Abrupt upper-plate tilting during slab-transition-zone collision. *Tectonophysics*, *746*, 199-211. Retrieved from `https://doi.org/10.1016/j.tecto.2017.09.013` doi: 10.1016/j.tecto.2017.09.013

Crameri, F., Schmeling, H., Golabek, G. J., Duretz, T., Orendt, R., Buiter, S. J. H., ... Tackley, P. J. (2012). A comparison of numerical surface topography calculations in geodynamic modelling: An evaluation of the 'sticky air' method. *Geophys. J. Int.*, *189*(1), 38–54. doi: 10.1111/j.1365-246X.2012.05388.x

Crameri, F., & Tackley, P. J. (2015). Parameters controlling dynamically self-consistent plate tectonics and single-sided subduction in global models of mantle convection. *Journal of Geophysical Research: Solid Earth*, *3*, 1-27. doi: 10.1002/2014JB011664.Abstract

Dannberg, J., Eilon, Z., Faul, U., Gassmöller, R., Moulik, P., & Myhill, R. (2017). The importance of grain size to mantle dynamics and seismological observations. *Geochemistry, Geophys. Geosystems*, *18*(8), 3034–3061. doi: 10.1002/2017GC006944

Faccenna, C., & Becker, T. W. (2010). Shaping mobile belts by small-scale convection. *Nature*, *465*, 602-605. Retrieved from `http://dx.doi.org/10.1038/nature09064` doi: 10.1038/nature09064

Fukao, Y., & Obayashi, M. (2013, nov). Subducted slabs stagnant above, penetrating through, and trapped below the 660 km discontinuity. *J. Geophys. Res. Solid Earth*, *118*(11), 5920–5938. Retrieved from `http://doi.wiley.com/10.1002/2013JB010466` doi: 10.1002/2013JB010466

Fukao, Y., Obayashi, M., & Nakakuki, T. (2009). Stagnant Slab: A Review. *Annu. Rev. Earth Planet. Sci.*, *37*(1), 19–46. Retrieved from `http://www.annualreviews.org/doi/10.1146/annurev.earth.36.031207.124224` doi: 10.1146/annurev.earth.36.031207.124224

Funiciello, F., Faccenna, C., Giardini, D., & Regenauer-Lieb, K. (2003). Dynamics of retreating slabs: 2. Insights from three-dimensional laboratory experiments. *J. Geophys. Res. Solid Earth*, *108*(B4), 1–16. Retrieved from `http://doi.wiley.com/10.1029/2001JB000896` doi: 10.1029/2001jb000896

Garel, F., Goes, S., Davies, D. R., Davies, J. H., Kramer, S. C., & Wilson, C. R. (2014, may). Interaction of subducted slabs with the mantle transition-zone: A regime diagram from 2-D thermo-mechanical models with a mobile trench and an overriding plate. *Geochemistry, Geophys. Geosystems*, *15*(5), 1739–1765. Retrieved from `https://onlinelibrary.wiley.com/doi/10.1002/2014GC005257` doi: 10.1002/2014GC005257

Goes, S., Agrusta, R., van Hunen, J., & Garel, F. (2017, 6). Subduction-transition zone interaction: A review. *Geosphere*, *13*, 644-664. doi: 10.1130/GES01476.1

Grima, A. G., Lithgow-Bertelloni, C., & Crameri, F. (2020, 10). Orphaning regimes: The missing link between flattened and penetrating slab morphologies. *Frontiers in Earth Science*, *8*, 1-19. Retrieved from `https://www.frontiersin.org/article/10.3389/feart.2020.00374/full` doi: 10.3389/feart.2020.00374

Hager, B. H. (1984). Constraints on Mantle Rheology and Flow Residual Geoid: degree 2-10. *J. Geophys. Res.*, *89*(4), 6003–6015.

Hager, B. H., & Richards, M. A. (1989). Long-wavelength variations in earth's geoid: physical models and dynamical implications. *Philosophical Transactions of the Royal Society of London. Series A, Mathematical and Physical Sciences*, *328*, 309-327. doi: 10.1098/rsta.1989.0038

Heilman, E., & Becker, T. W. (2022). Plume-Slab Interactions Can Shut Off Subduction. *Geophys. Res. Lett.*, *49*(13), 1–9. doi: 10.1029/2022GL099286

Heuret, A., & Lallemand, S. (2005, 3). Plate motions, slab dynamics and back-arc deformation. *Physics of the Earth and Planetary Interiors*, *149*, 31-51. Retrieved from `https://linkinghub.elsevier.com/retrieve/pii/S0031920104003462` doi: 10.1016/j.pepi.2004.08.022

Holt, A. F., Becker, T. W., & Buffett, B. A. (2015, 4). Trench migration and overriding plate stress in dynamic subduction models. *Geophysical Journal International*, *201*, 172-192. doi: 10.1093/gji/ggv011

Holt, A. F., Buffett, B. A., & Becker, T. W. (2015, 5). Overriding plate thickness control on subducting plate curvature. *Geophysical Research Letters*, *42*, 3802-3810. doi: 10.1002/2015GL063834

Hosseini, K., Matthews, K. J., Sigloch, K., Shephard, G. E., Domeier, M., & Tsekhmistrenko, M. (2018). Submachine: Web-based tools for exploring seismic tomography and other models of earth's deep interior. *Geochemistry, Geophysics, Geosystems*, *19*, 1464-1483. doi: 10.1029/2018GC007431

King, S. D., & Masters, G. (1992). Scott D. King x and Guy Masters. *Geophys. Res. Lett.*, *19*(15), 1551–1554.

Lu, C., Grand, S. P., Lai, H., & Garnero, E. J. (2019, 11). Tx2019slab: A new p and s tomography model incorporating subducting slabs. *Journal of Geophysical Research: Solid Earth*, *124*, 11549-11567. doi: 10.1029/2019JB017448

Mitrovica, J. X., & Forte, A. M. (2001). Deep-mantle high-viscosity flow and thermochemical structure inferred from seismic and geodynamic data. *Nature*, *410*, 1049–1056.

Mitrovica, J. X., & Forte, A. M. (2004). A new inference of mantle viscosity based upon joint inversion of convection and glacial isostatic adjustment data. *Earth Planet. Sci. Lett.*, *225*(1-2), 177–189. doi: 10.1016/j.epsl.2004.06.005

Montési, L. G. J. (2013). Fabric development as the key for forming ductile shear zones and enabling plate tectonics. *J. Struct. Geol.*, *50*, 254–266.

Naliboff, J. B., Conrad, C. P., & Lithgow-Bertelloni, C. (2009, 11). Modification of the lithospheric stress field by lateral variations in plate-mantle coupling. *Geophysical Research Letters*, *36*. doi: 10.1029/2009GL040484

Rudolph, M. L., Lekić, V., & Lithgow-Bertelloni, C. (2015). Viscosity jump in Earth's mid-mantle. *Science*, *350*(6266), 1349–1352. Retrieved from `http://science.sciencemag.org/content/350/6266/1349.abstract` doi: 10.1126/science.aad1929

Rudolph, M. L., Moulik, P., & Lekić, V. (2020). Bayesian Inference of Mantle Viscosity From Whole-Mantle Density Models. *Geochemistry, Geophys. Geosystems*, *21*(11). doi: 10.1029/2020GC009335

Sharples, W., Jadamec, M. A., Moresi, L. N., & Capitanio, F. A. (2014, 8). Overriding plate controls on subduction evolution. *Journal of Geophysical Research: Solid Earth*, *119*, 6684-6704. Retrieved from `https://onlinelibrary.wiley.com/doi/abs/10.1002/2014JB011163` doi: 10.1002/2014JB011163

Stegman, D. R., Freeman, J., Schellart, W. P., Moresi, L. N., & May, D. (2006). Influence of trench width on subduction hinge retreat rates in 3-D models of slab rollback. *Geochem., Geophys., Geosys.*, *7*. doi: 10.1029/2005GC001056

Summeren, J. V., Conrad, C. P., & Lithgow-Bertelloni, C. (2012). The importance of slab pull and a global asthenosphere to plate motions. *Geochemistry, Geophysics, Geosystems*, *13*, 1-13. doi: 10.1029/2011GC003873

Tackley, P. J. (2000). Self-consistent generation of tectonic plates in time dependent, three-dimensional mantle convection simulations 1. Pseudoplastic yielding. *Geochemistry Geophys. Geosystems*, *1*.

Tackley, P. J. (2008). Modelling compressible mantle convection with large viscosity contrasts in a three-dimensional spherical shell using the yin-yang grid. *Phys. Earth Planet. Inter.*, *171*(1-4), 7–18. doi: 10.1016/j.pepi.2008.08.005

Turcotte, D. L., & Schubert, G. (2014). *Geodynamics.* doi: 10.1017/CBO9780511807442

Van Zelst, I., Crameri, F., Pusok, A. E., Glerum, A., Dannberg, J., & Thieulot, C. (2022). 101 geodynamic modelling: How to design, interpret, and communicate numerical studies of the solid Earth. *Solid Earth*, *13*(3), 583–637. doi: 10.5194/se-13-583-2022

Willingshofer, E., Sokoutis, D., Luth, S. W., Beekman, F., & Cloetingh, S. (2013). Subduction and deformation of the continental lithosphere in response to plate and crust-mantle coupling. *Geology*, *41*, 1239-1242. doi: 10.1130/G34815.1

Zahirovic, S., Müller, R. D., Seton, M., & Flament, N. (2015, 5). Tectonic speed limits from plate kinematic reconstructions. *Earth and Planetary Science Letters*, *418*, 40-52. doi: 10.1016/j.epsl.2015.02.037

Zhong, S. (2001). Role of ocean-continent contrast and continental keels on plate motion, net rotation of lithosphere, and the geoid. *Journal of Geophysical Research: Solid Earth*, *106*, 703-712. doi: 10.1029/2000jb900364

Zhong, S., & Gurnis, M. (1995). Mantle convection with plates and mobile, faulted plate margins. *Science*, *267*, 838-842.

Figure 1.

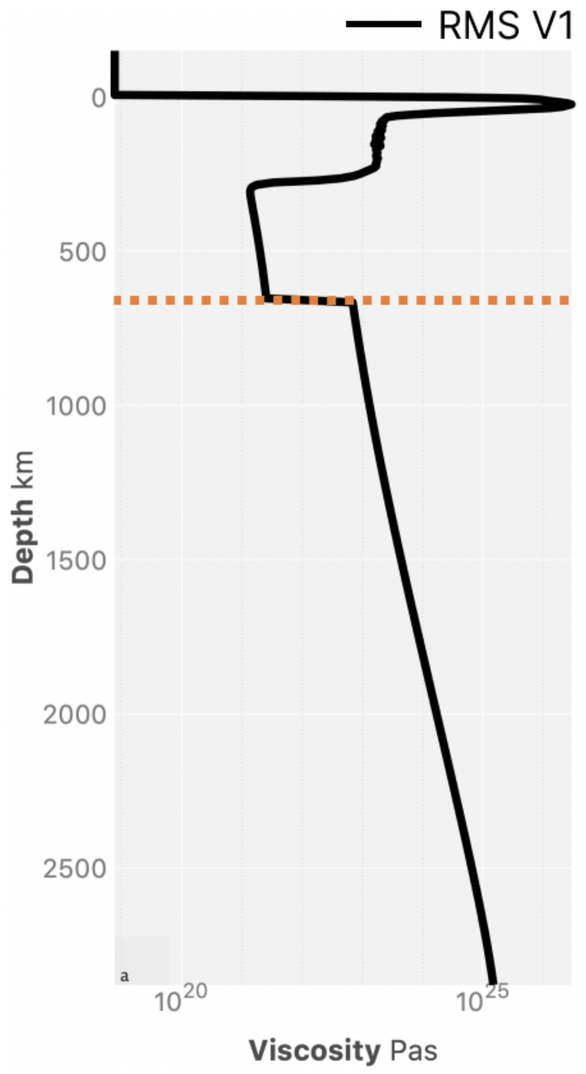
RMS V1
0
500
1000
1500
2000
2500
Depth km
a
10^{20}
10^{25}
Viscosity Pas

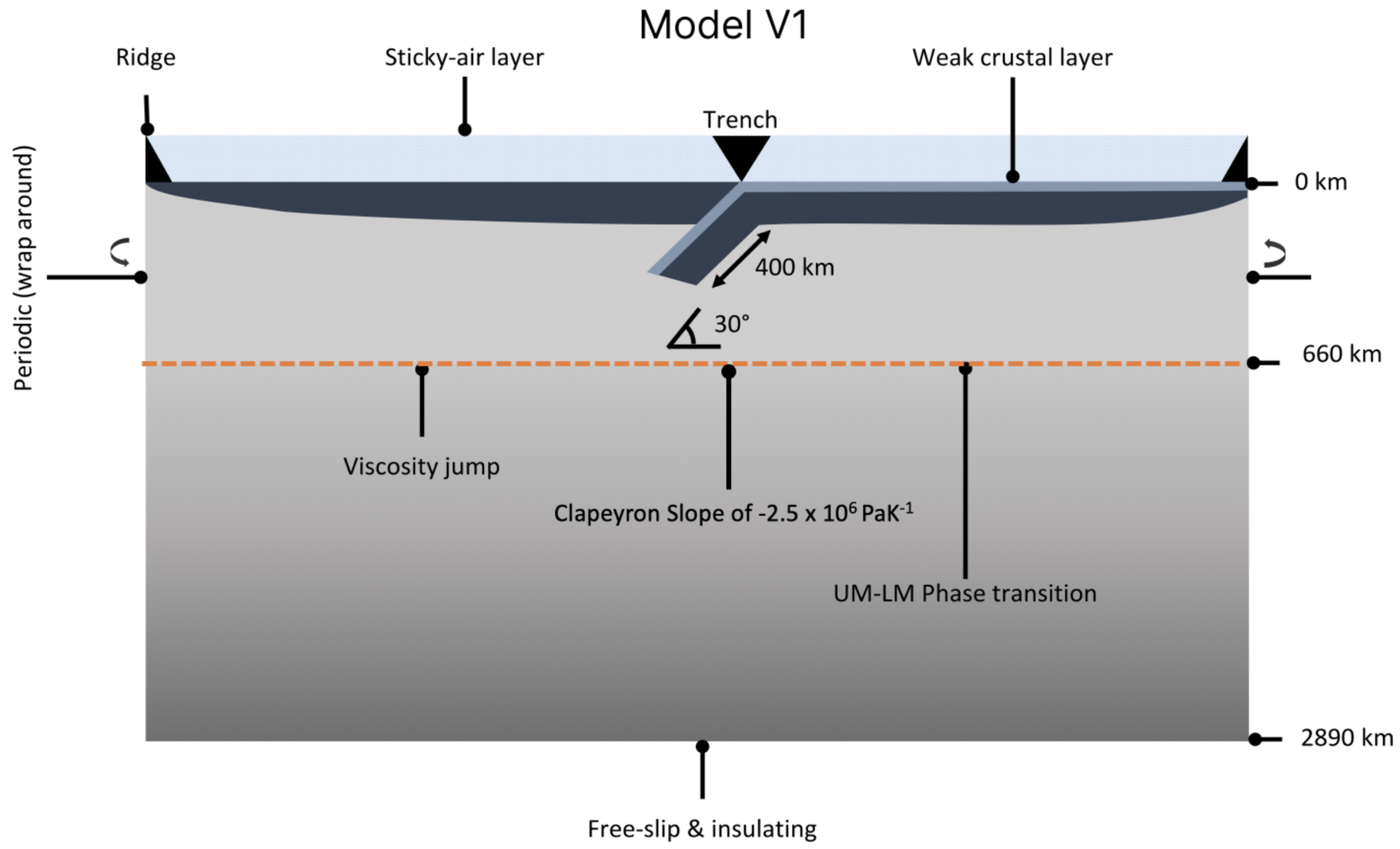
Model V1
Ridge
Sticky-air layer
Weak crustal layer
Trench
0 km
400 km
30°
660 km
Periodic (wrap around)
Viscosity jump
Clapeyron Slope of -2.5 x 10^6 PaK^{-1}
UM-LM Phase transition
2890 km
Free-slip & insulating

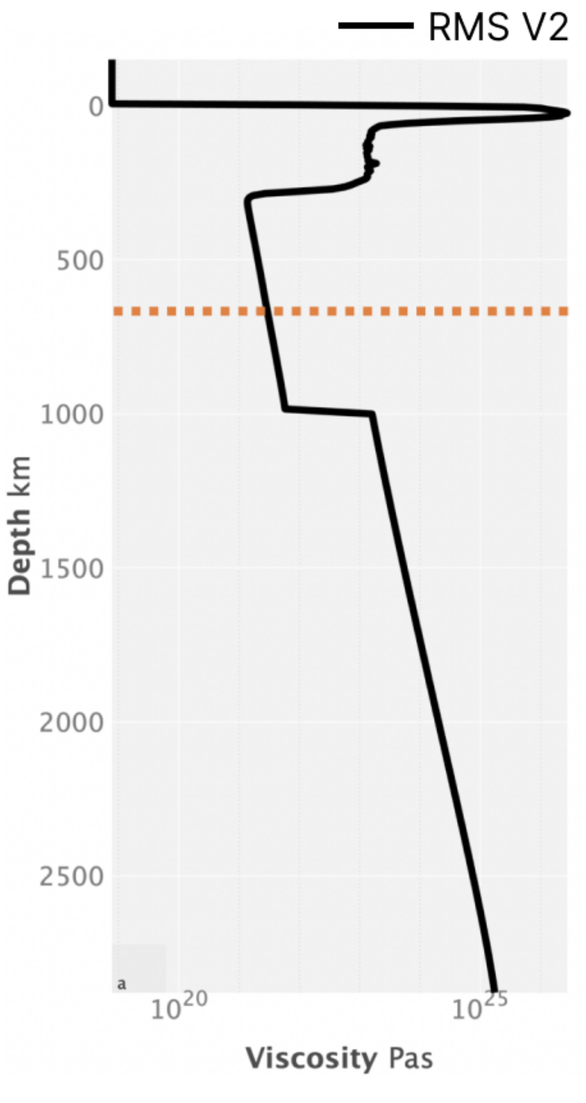
RMS V2
0
500
1000
1500
2000
2500
Depth km
a
10^{20}
10^{25}
Viscosity Pas

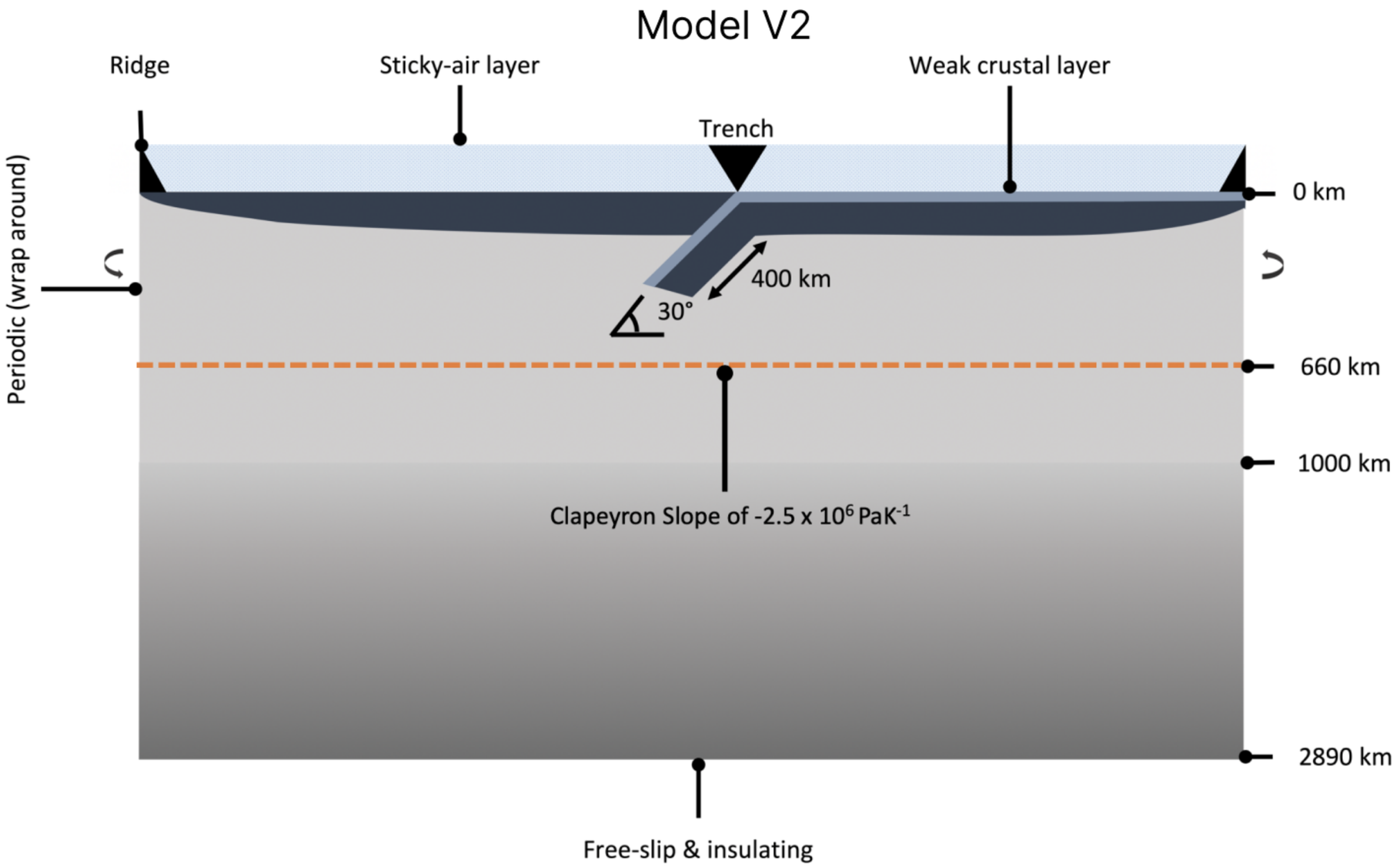
Model V2
Ridge
Sticky-air layer
Weak crustal layer
Trench
0 km
400 km
30°
660 km
1000 km
Periodic (wrap around)
Clapeyron Slope of -2.5 x 10^6 PaK^{-1}
2890 km
Free-slip & insulating

Figure 2.

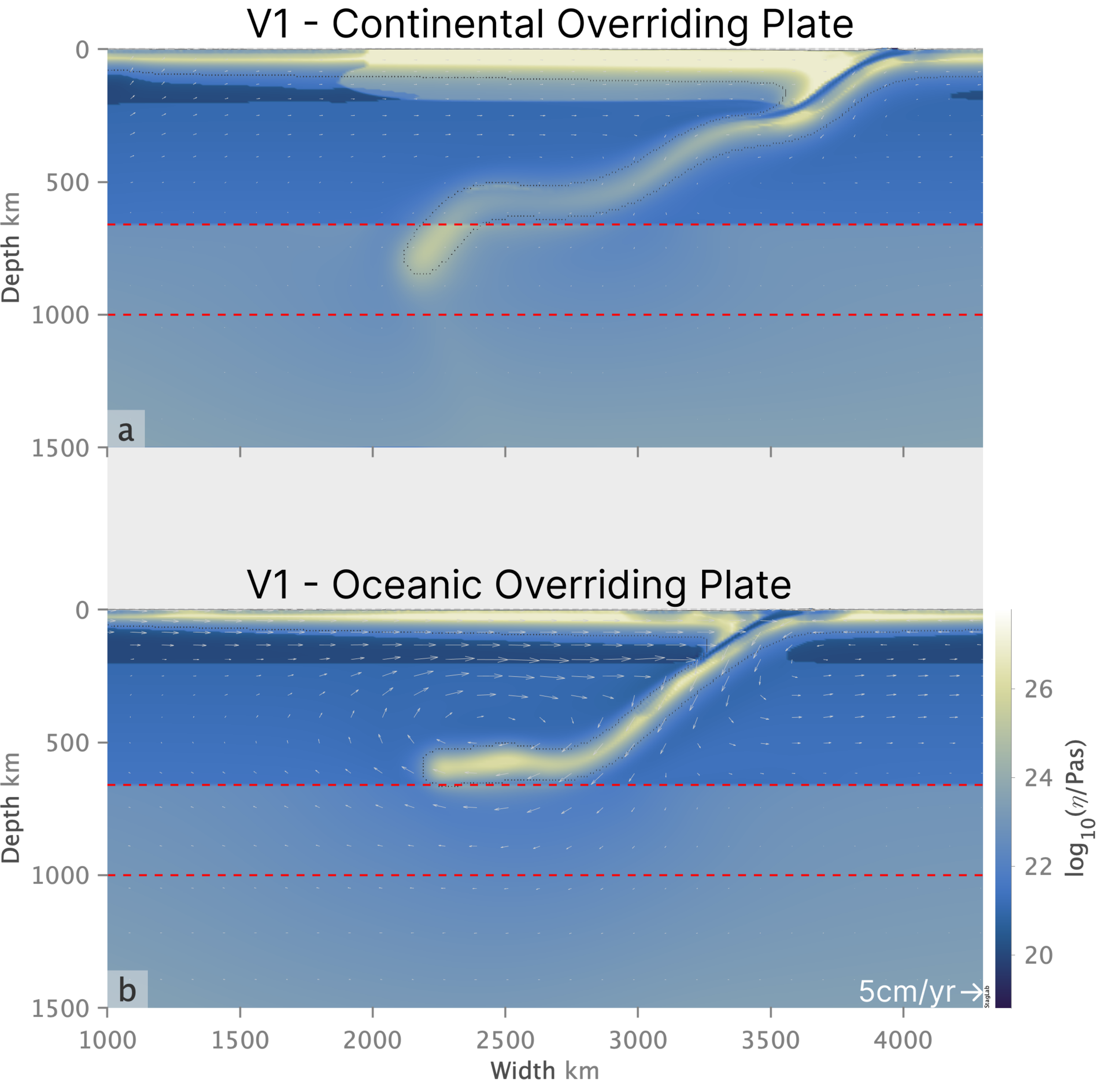
V1 - Continental Overriding Plate
0
500
1000
1500
Depth km
a
V1 - Oceanic Overriding Plate
0
500
1000
1500
Depth km
b
5cm/yr
StagLab
26
24
22
20
$\log_{10}(\eta/\mathrm{Pas})$
1000
1500
2000
2500
3000
3500
4000
Width km

Figure 3.

V2 - Continental Overriding Plate

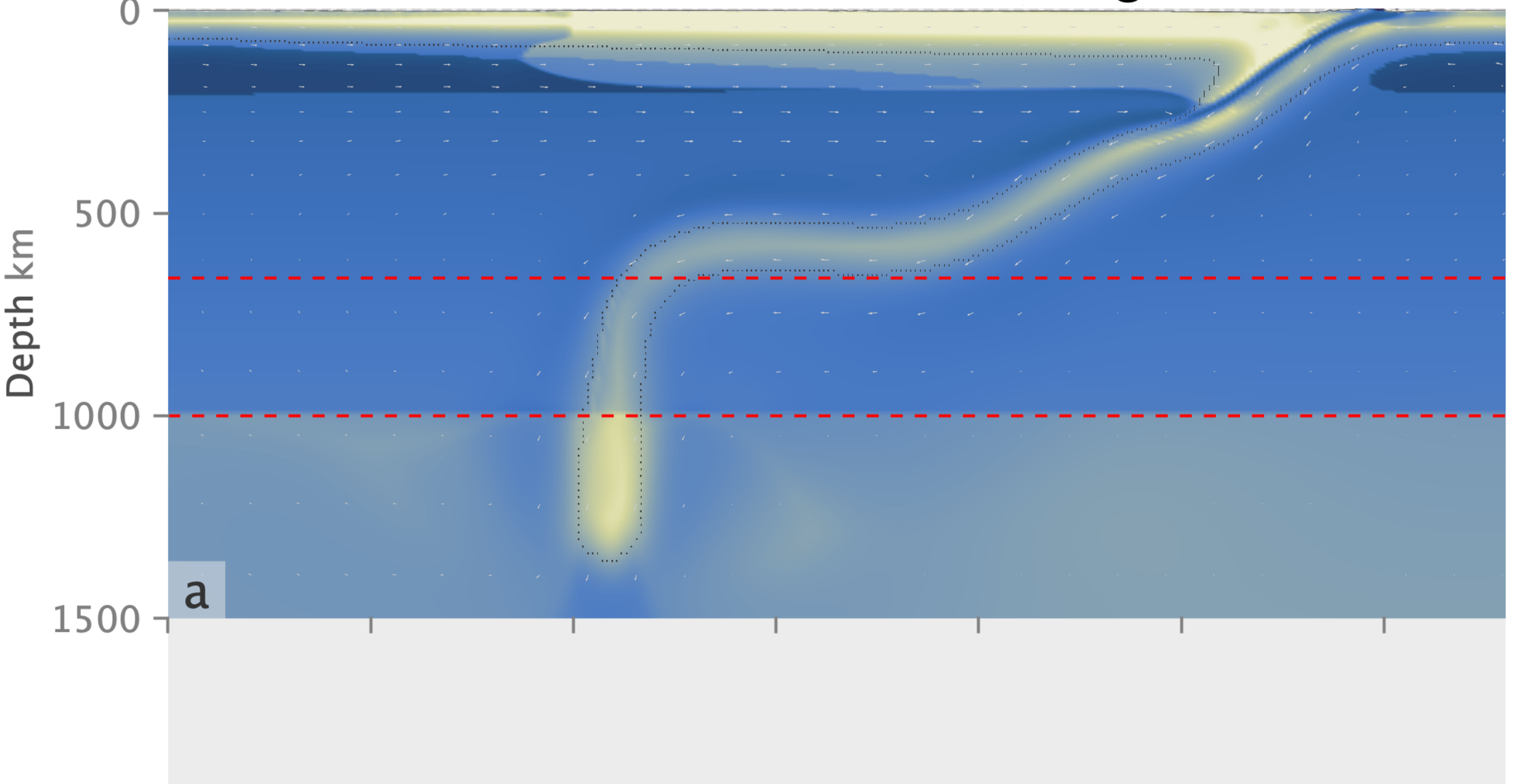

V2 - Oceanic Overriding Plate

Figure 4.

Trench Velocity and Slab Tip Angle for V1 with Continent

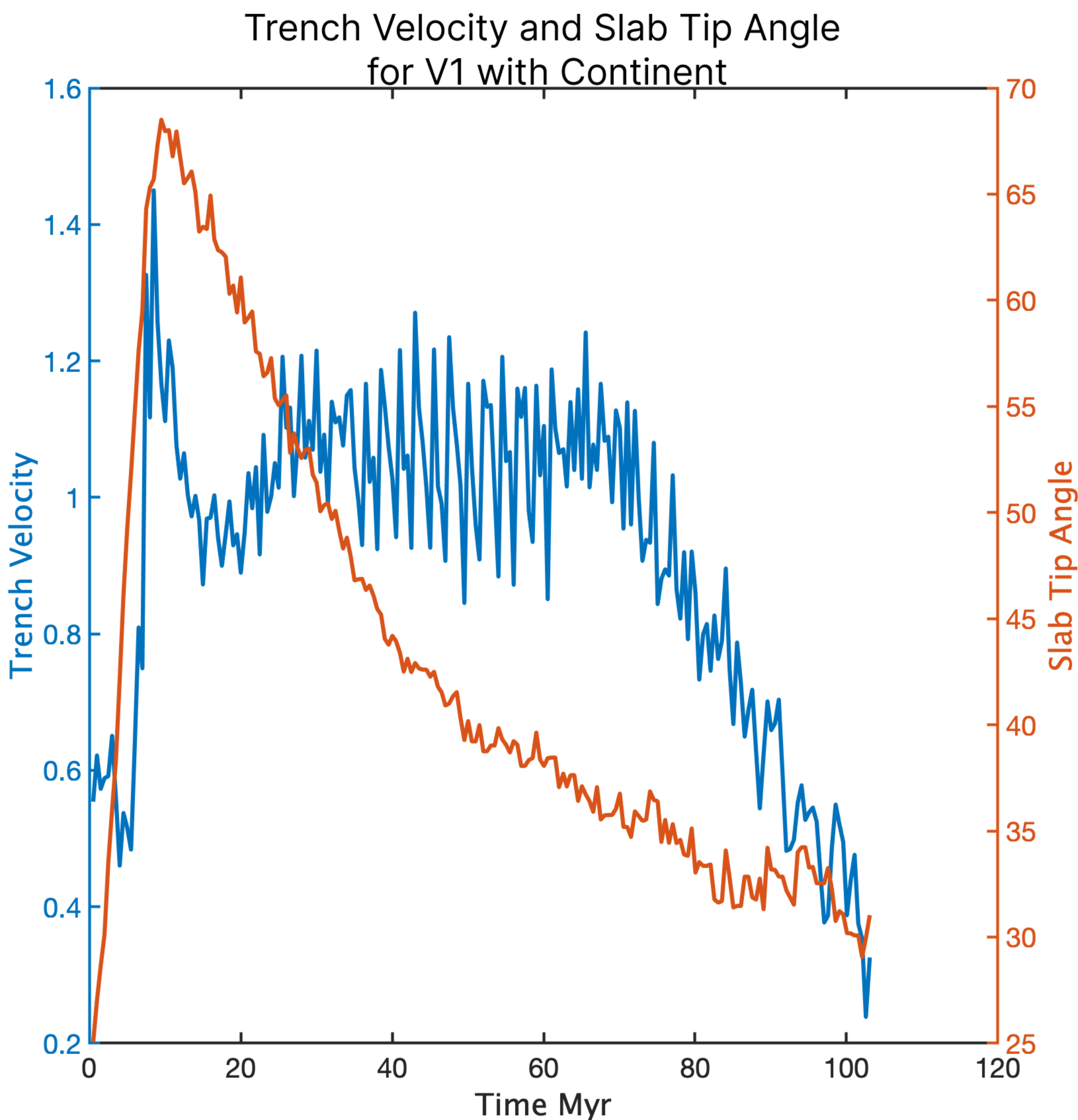

Figure 5.

Trench Velocity and Slab Tip Angle for V2 with Continent

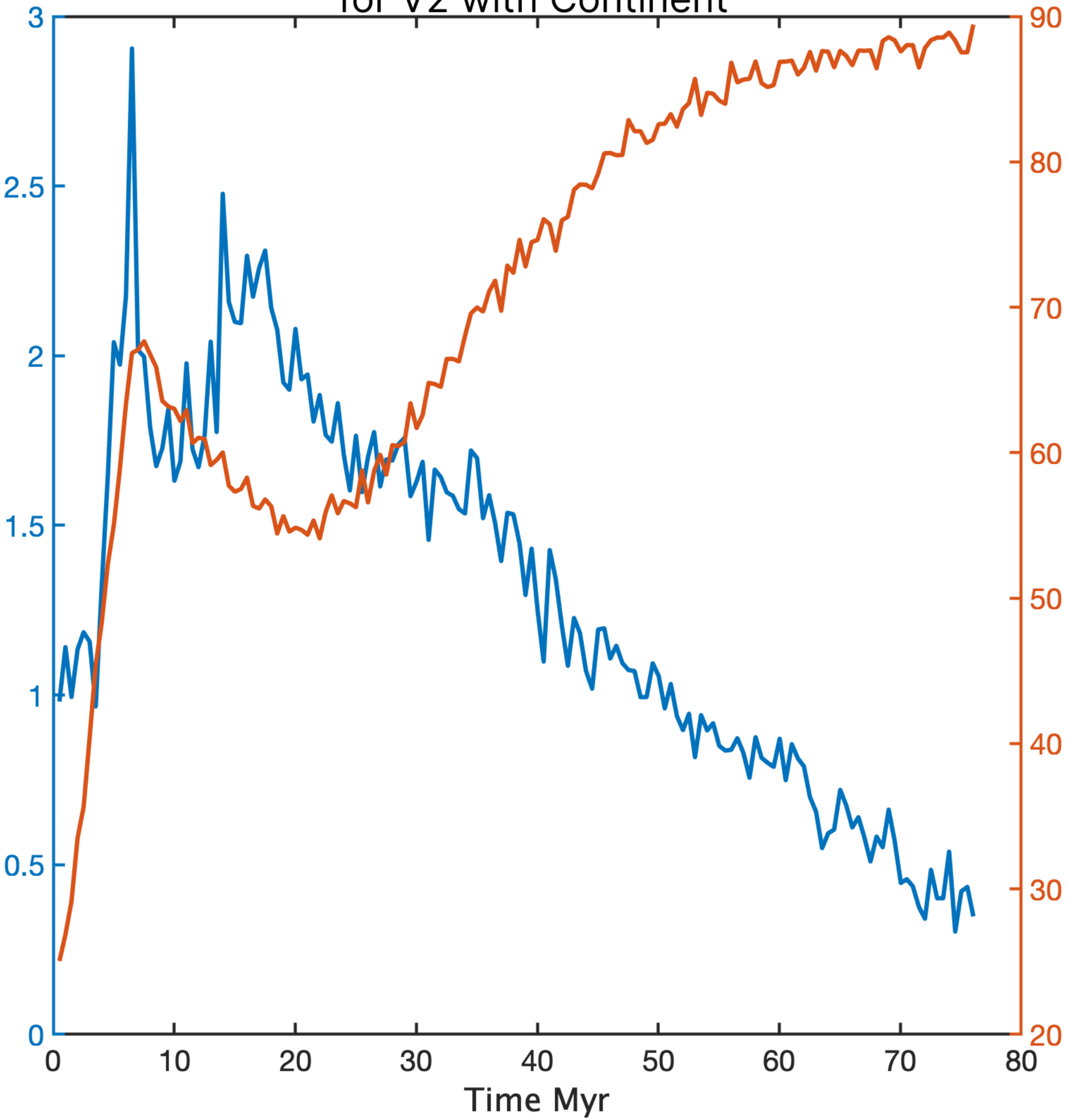

Figure 6.

a. Vertical Sinking Stage

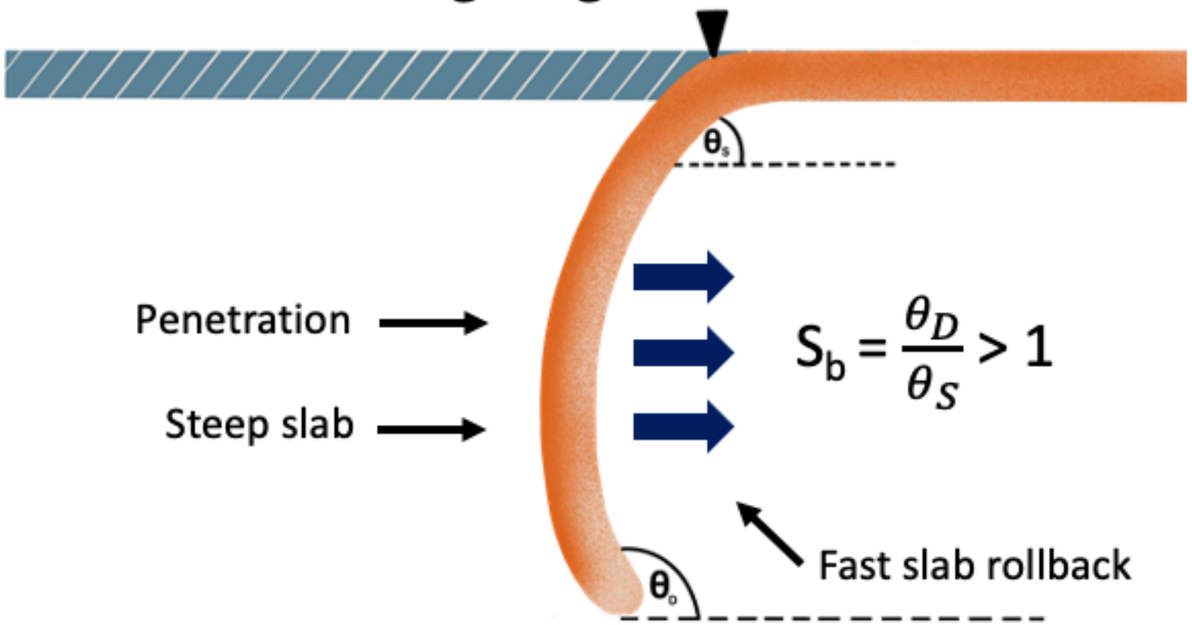

b. Deformation Stage

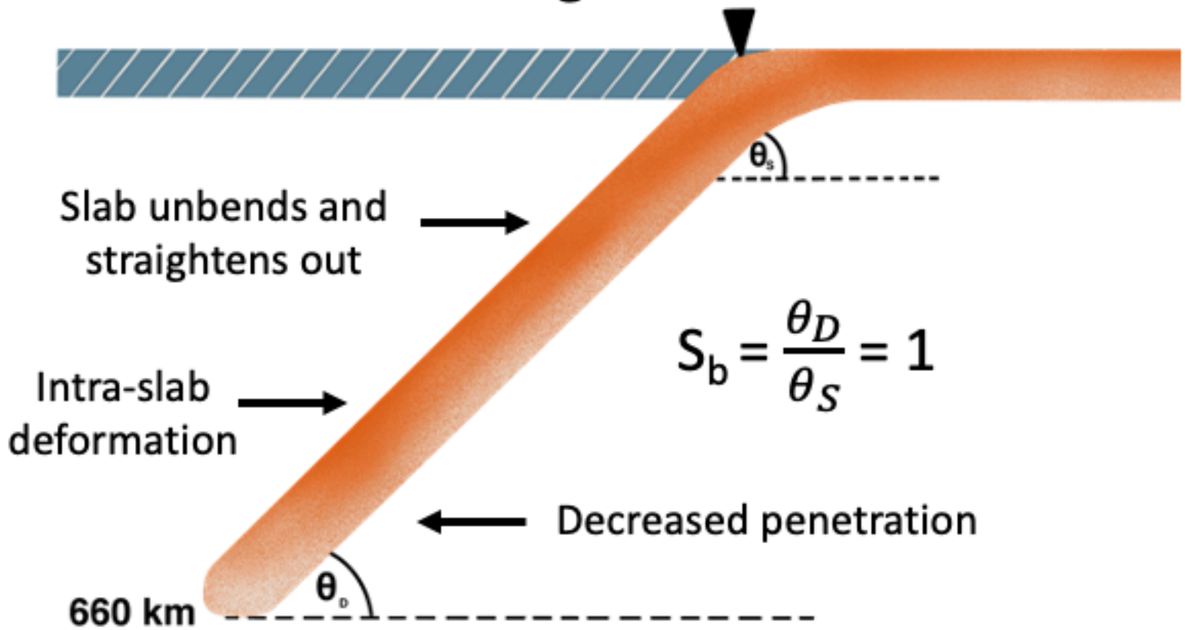

c. Flattened Stage

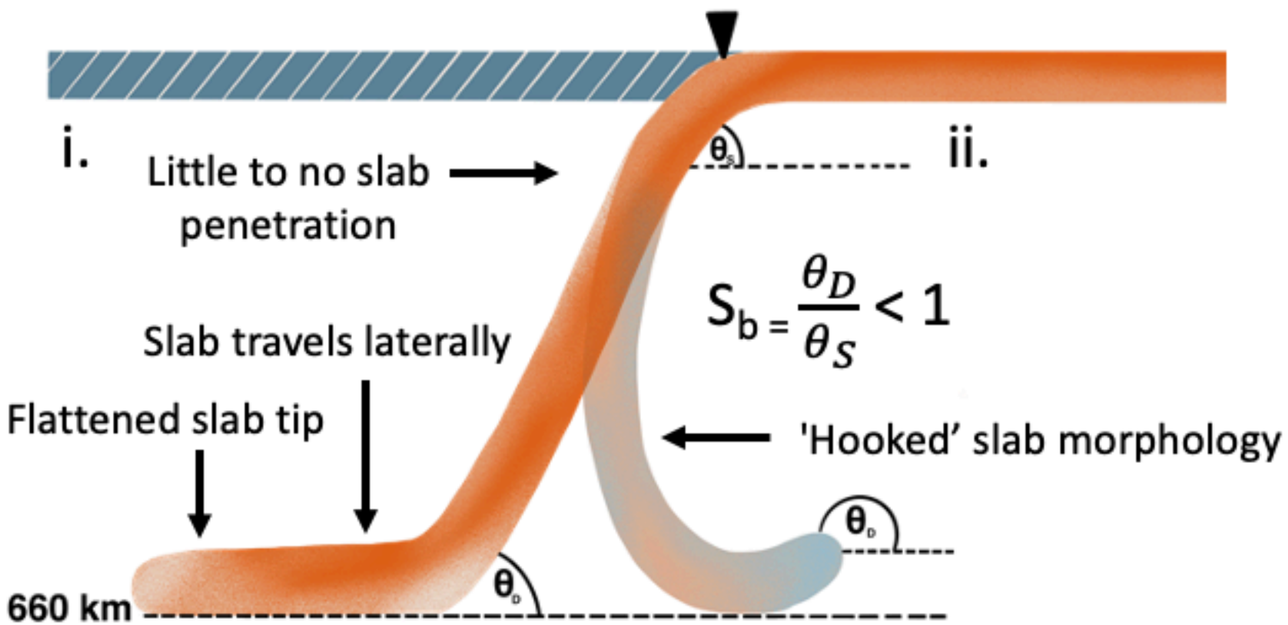

d. Renewal Stage

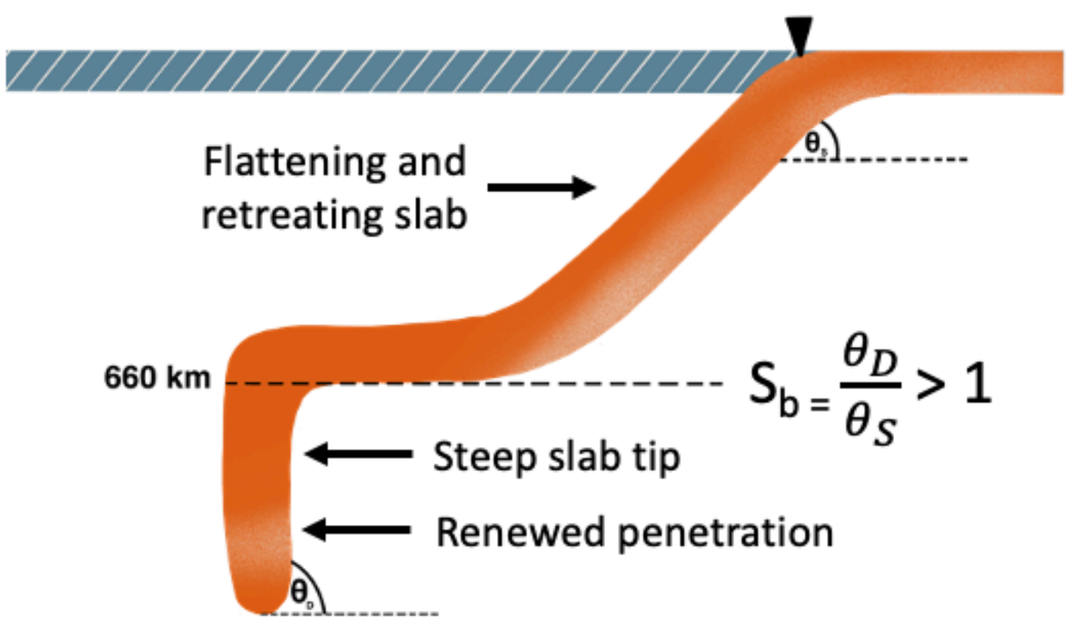

Figure 7.

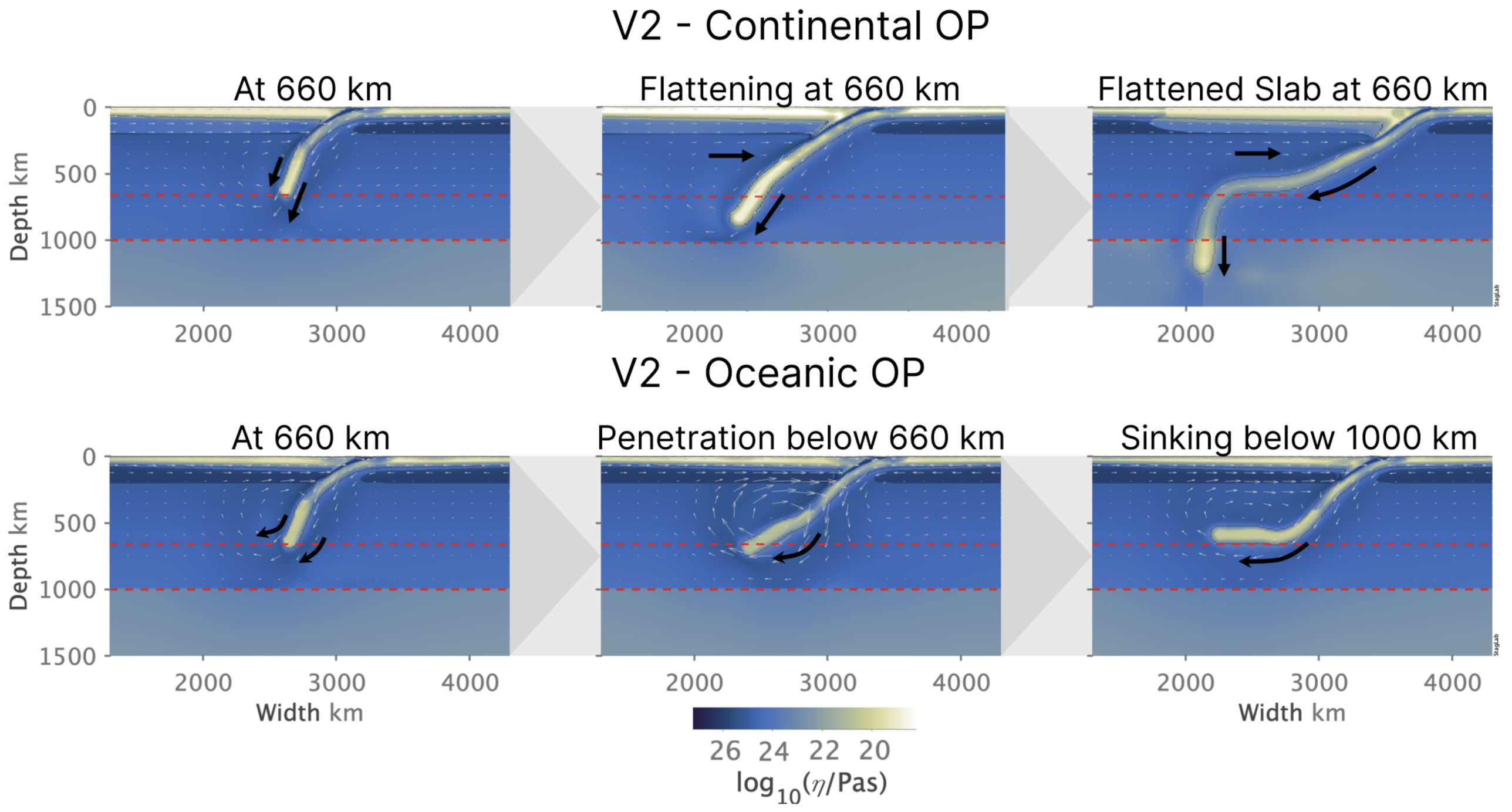
V2 - Continental OP
At 660 km
Flattening at 660 km
Flattened Slab at 660 km
V2 - Oceanic OP
At 660 km
Penetration below 660 km
Sinking below 1000 km
Depth km
0
500
1000
1500
2000
3000
4000
Width km
26 24 22 20
log10(η/Pas)

Figure 8.

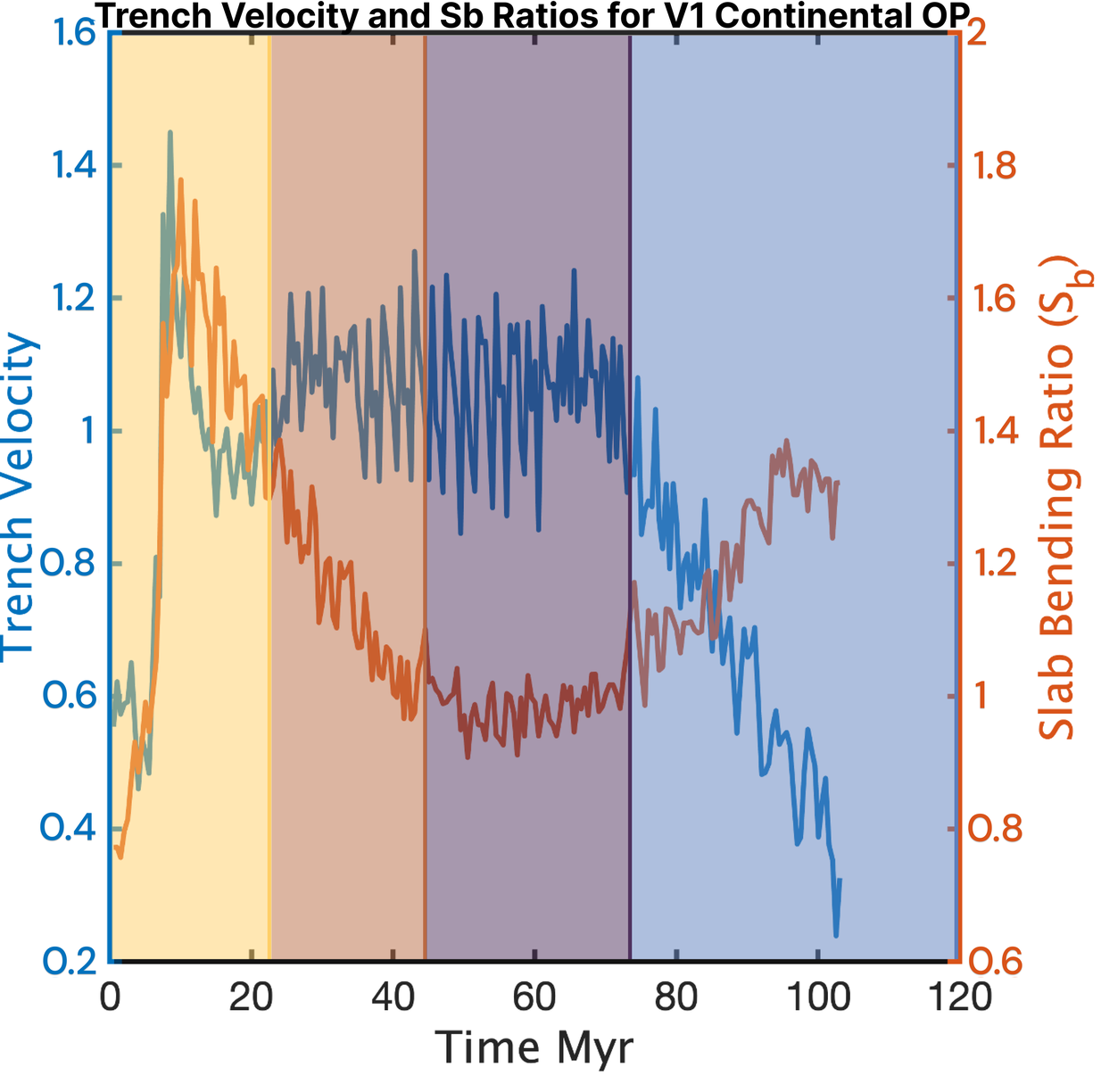
Trench Velocity and Sb Ratios for V1 Continental OP
Trench Velocity
Slab Bending Ratio (S_b)
Time Myr
0
20
40
60
80
100
120
0.2
0.4
0.6
0.8
1
1.2
1.4
1.6
0.6
0.8
1
1.2
1.4
1.6
1.8
2

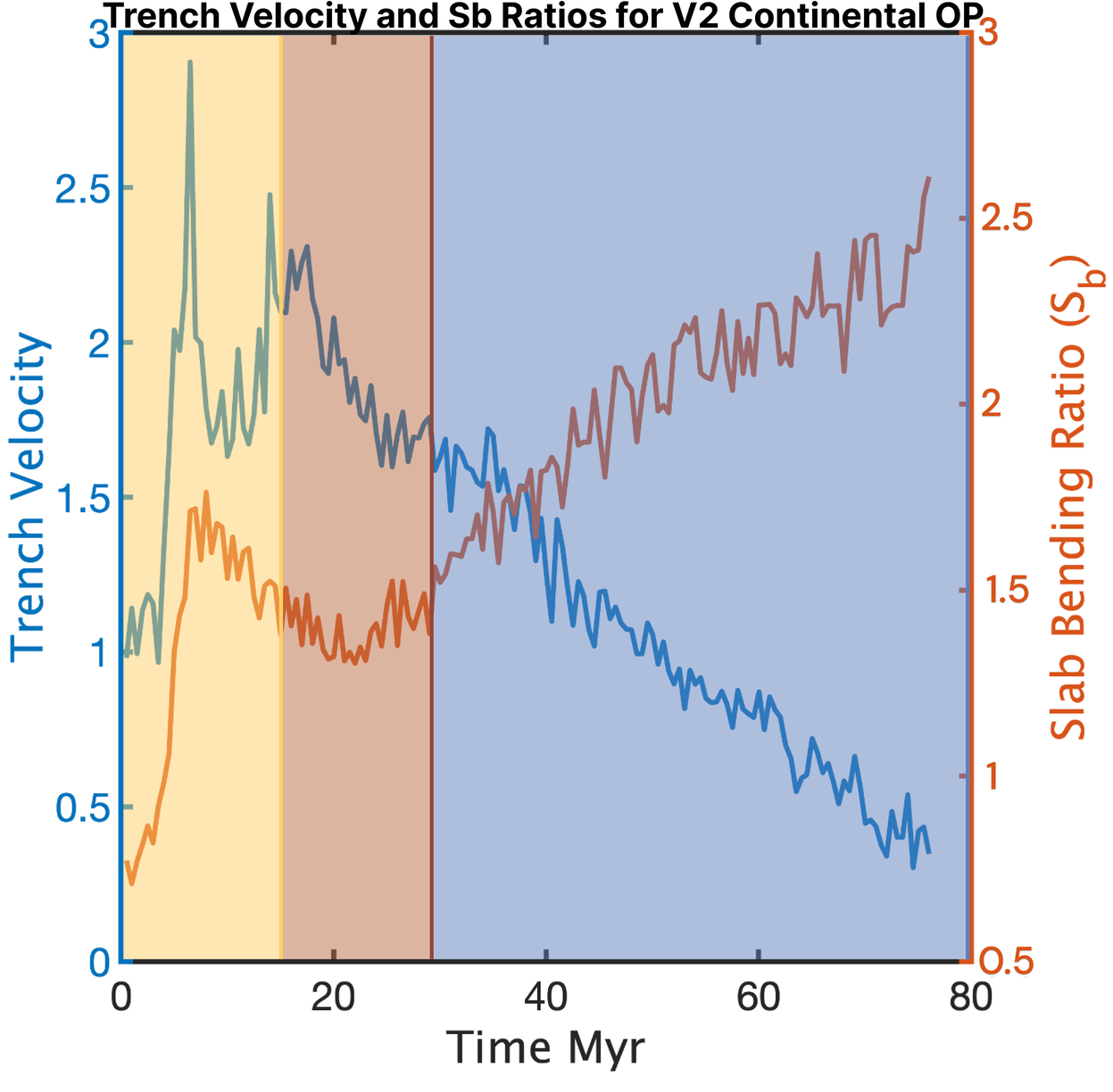
Trench Velocity and Sb Ratios for V2 Continental OP
Trench Velocity
Slab Bending Ratio (S_b)
Time Myr
0
20
40
60
80
0
0.5
1
1.5
2
2.5
3
0.5
1
1.5
2
2.5
3

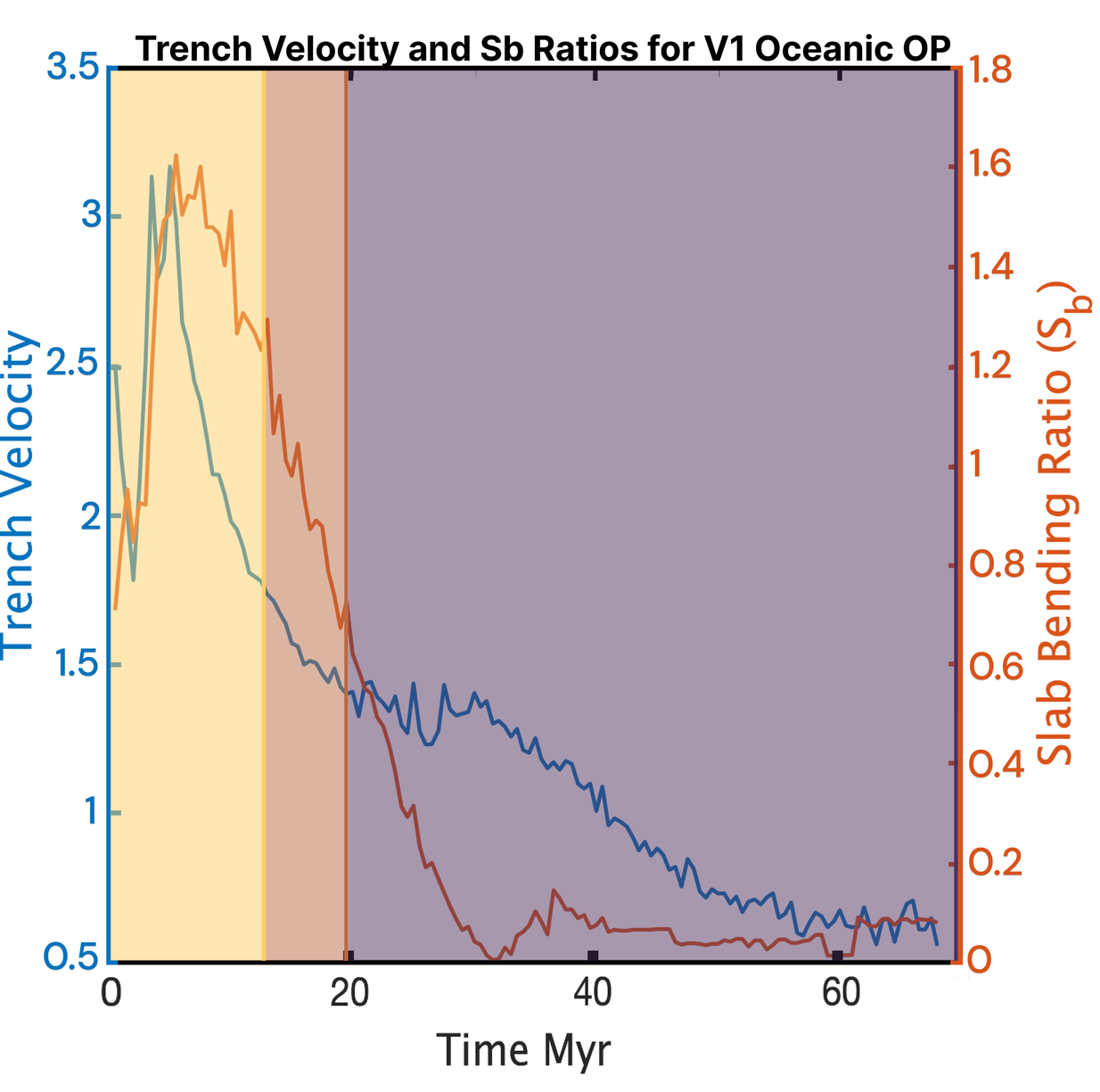
Trench Velocity and Sb Ratios for V1 Oceanic OP
Trench Velocity
Slab Bending Ratio (S_b)
Time Myr
0
20
40
60
0.5
1
1.5
2
2.5
3
3.5
0
0.2
0.4
0.6
0.8
1
1.2
1.4
1.6
1.8

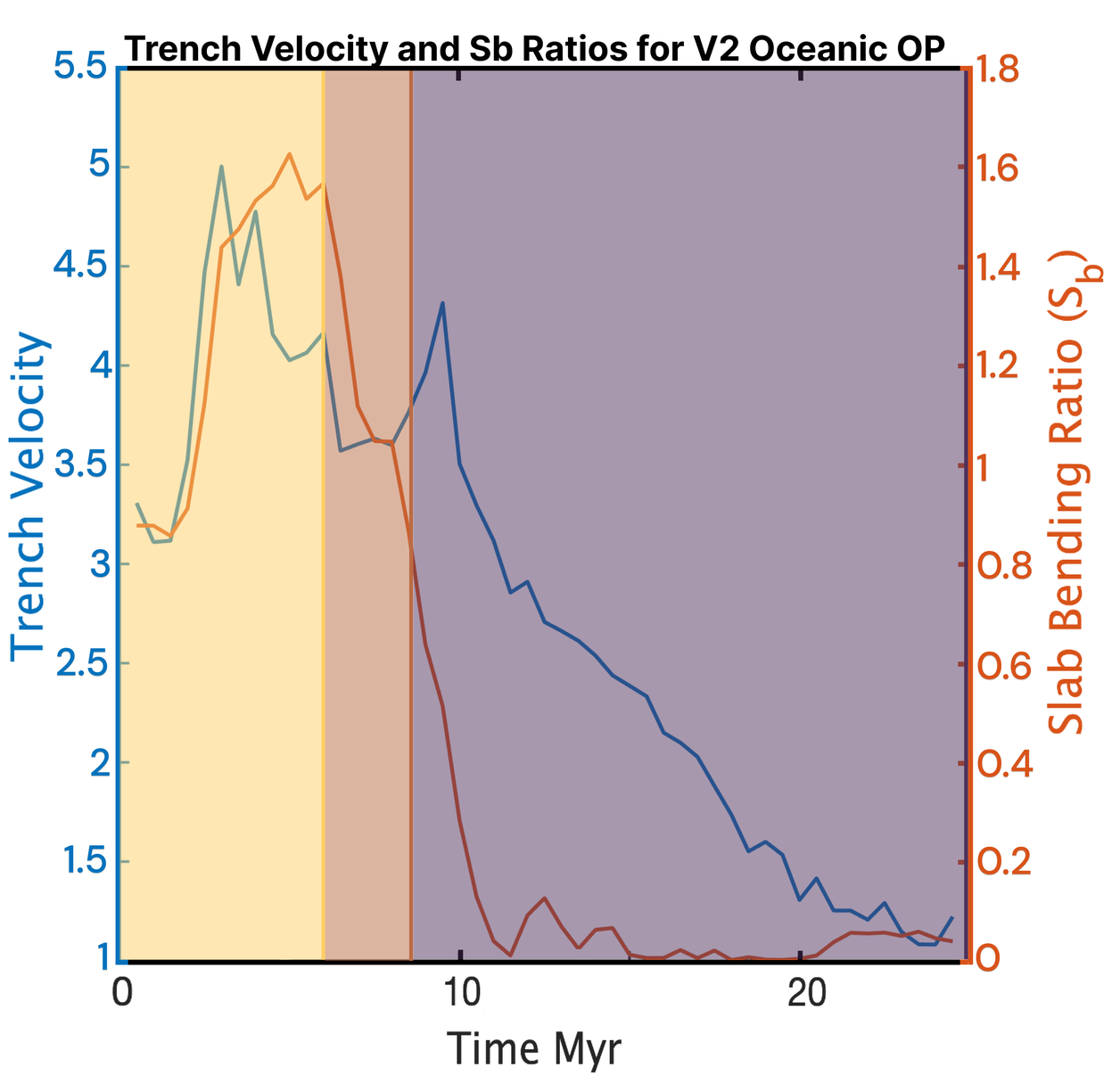
Trench Velocity and Sb Ratios for V2 Oceanic OP
Trench Velocity
Slab Bending Ratio (S_b)
Time Myr
0
10
20
1
1.5
2
2.5
3
3.5
4
4.5
5
5.5
0
0.2
0.4
0.6
0.8
1
1.2
1.4
1.6
1.8

Figure 9.

South Peruvian Arc
Slab deflection and penetration

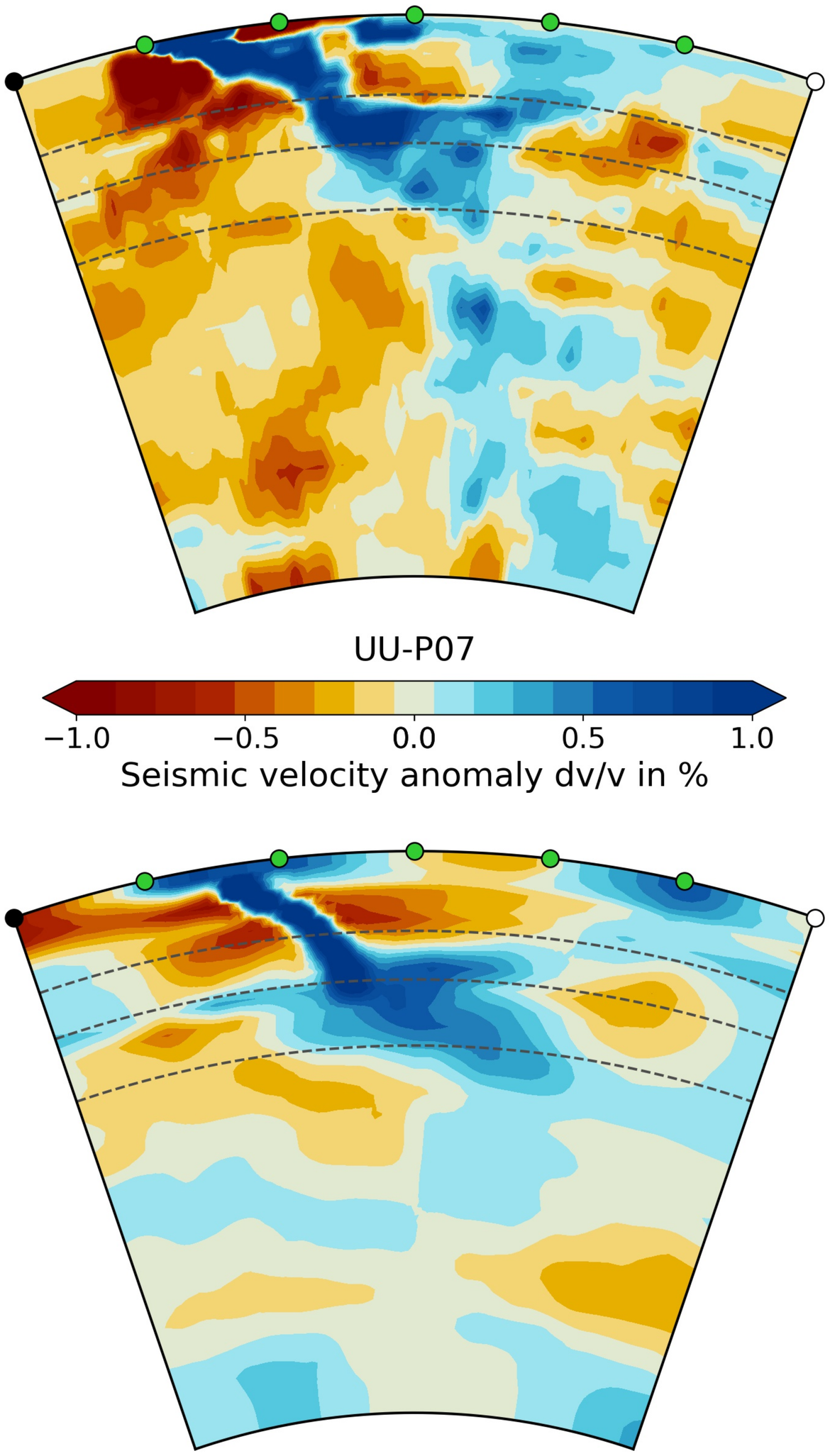

UU-P07

TX2019slab-P

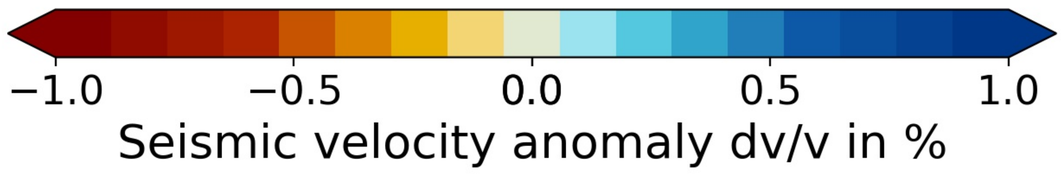

Izu-Bonin
Slab deflection

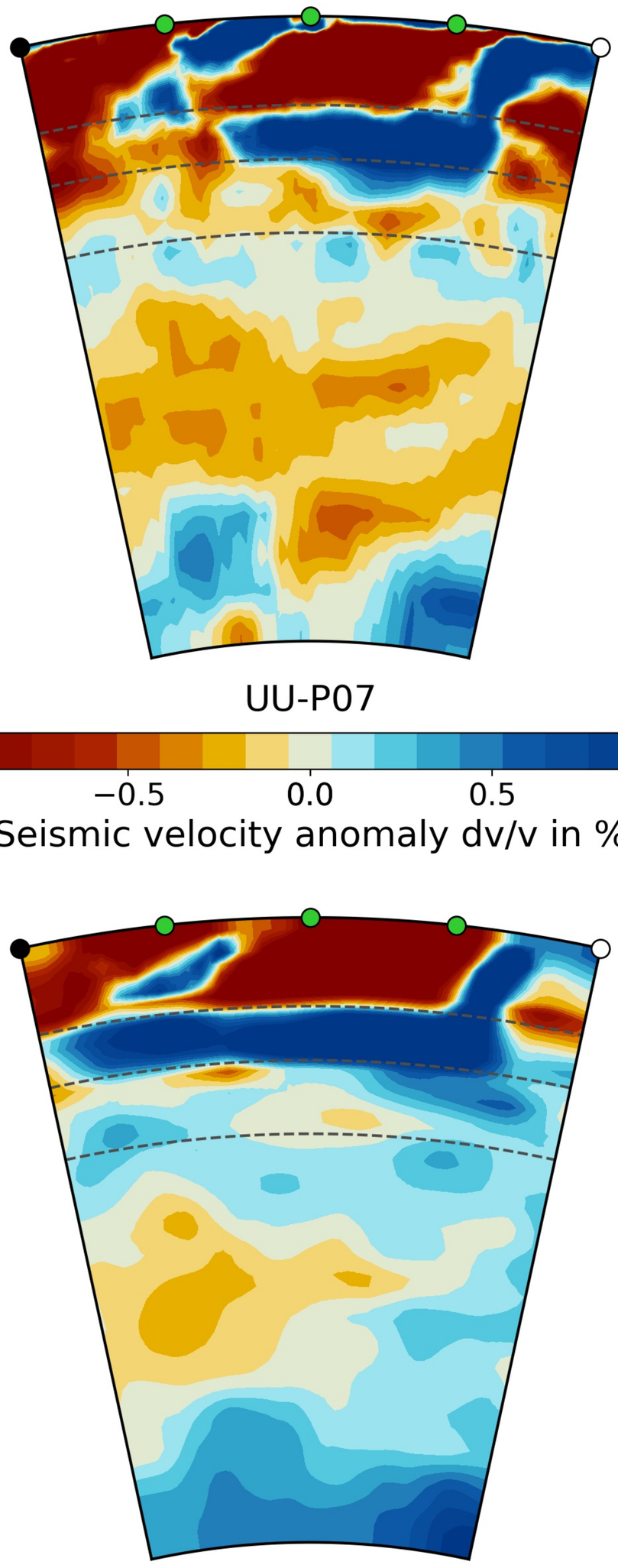

UU-P07

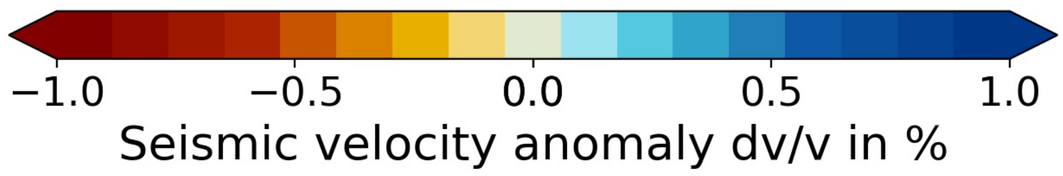

TX2019slab-P

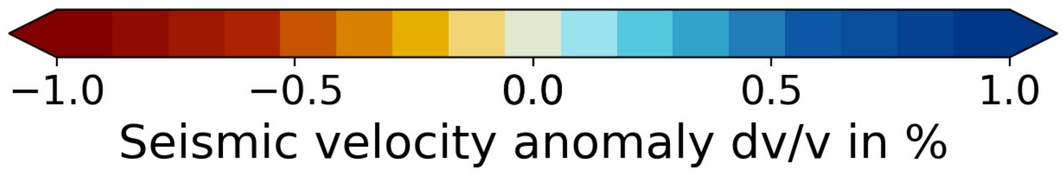

Figure A1.

V2 - Continental OP

0
500
1000
1500
Depth km
a

V2 - Oceanic OP

0
500
1000
1500
Depth km
b

1000
1500
2000
2500
3000
3500
4000
Width km

3700
3600
3500
3400
3300
3200
kg/m^3

StagLab

Figure A2.

Trench Velocity and Slab Tip Angle for V1 with Oceanic OP

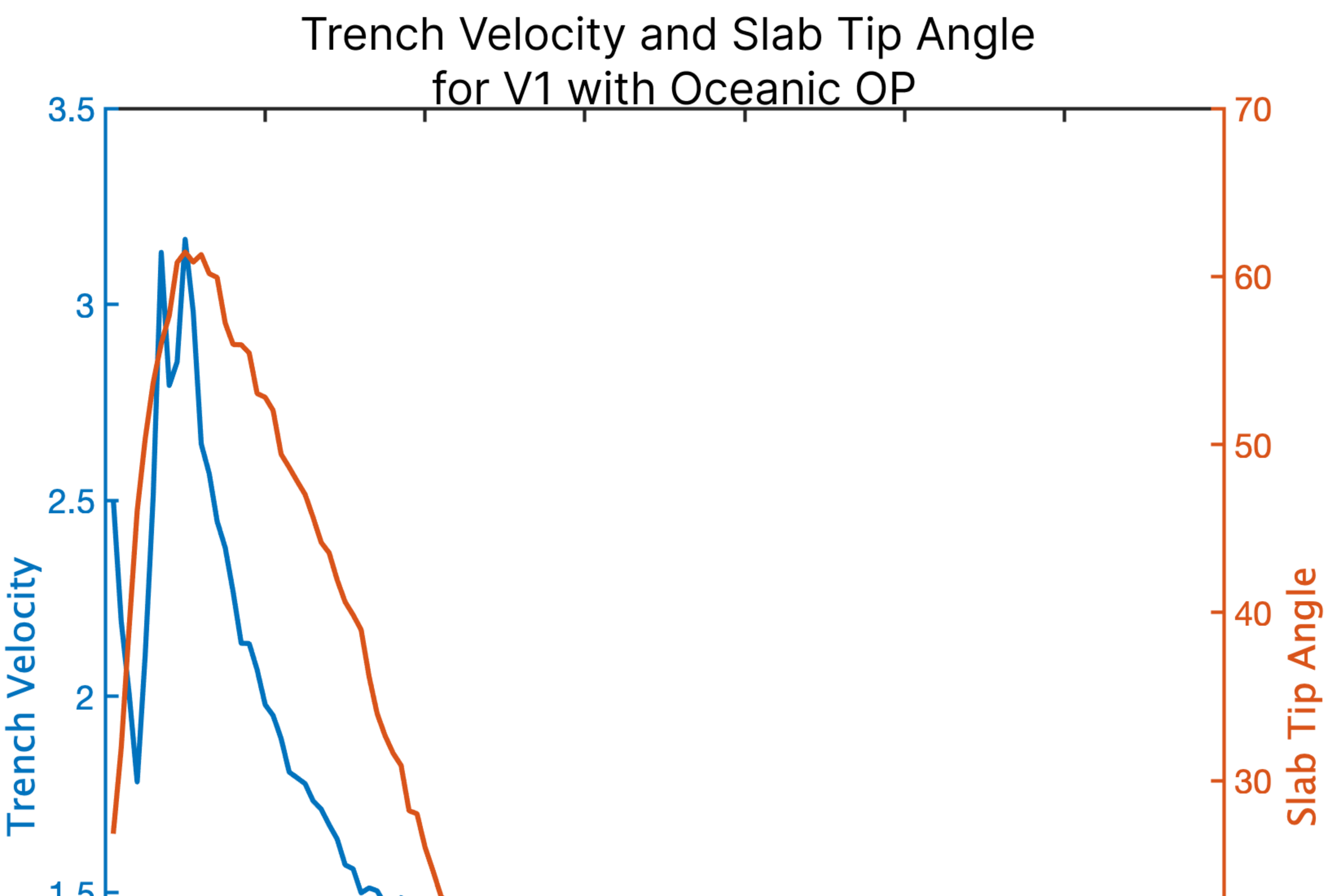

Figure A3.

Trench Velocity and Slab Tip Angle for V2 with Oceanic OP

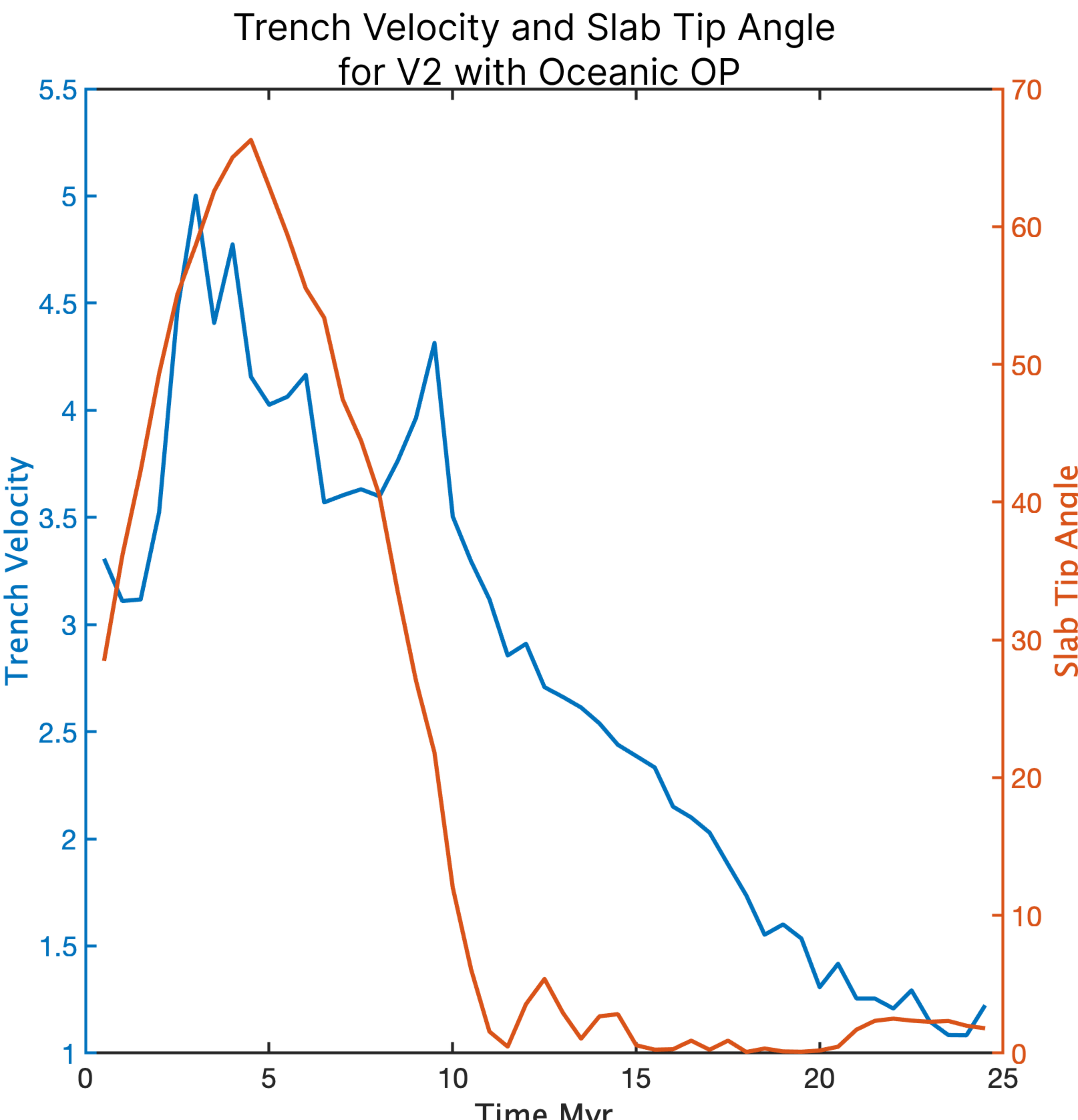

Figure A4.

V3 - Continental Overriding Plate

0
500
1000
1500
2000
2500
Depth km

a

V3 - Oceanic Overriding Plate

0
500
1000
1500
2000
2500

b

5cm/yr→

StagLab

1000
2000
3000
4000
5000
6000
Width km

26
24
22
20
$\log_{10}(\eta/\mathrm{Pas})$